CORNICHON HOMOLOG 5-dependent ER export of membrane cargoes in phosphate-starved *Arabidopsis* root as revealed by membrane proteomic analysis

Tzu-Yin Liu,[1,2,3,†] Ming-Hsuan Tsai,[1,†] Jhih-Yi Wang,[1,†] Hui-Fang Lung,[1] Chang-Yi Chiu,[1] Hong-Xuan Chow,[1] Chiao-An Lu[3]

[1]Institute of Bioinformatics and Structural Biology, College of Life Sciences and Medicine, National Tsing Hua University, Hsinchu 30013, Taiwan.

[2]Department of Life Science, College of Life Sciences and Medicine, National Tsing Hua University, Hsinchu 30013, Taiwan.

[3]Interdisciplinary Program of Life Science and Medicine, College of Life Sciences and Medicine, National Tsing Hua University, Hsinchu 30013, Taiwan.

Author for correspondence: Tzu-Yin Liu

Tel: +886 3 574-2096; Fax: +886 3 571-5934

Email: tzliu@life.nthu.edu.tw

Institute of Bioinformatics and Structural Biology, College of Life Sciences and Medicine, National Tsing Hua University, Hsinchu 30013, Taiwan

[†]These authors have contributed equally to this work.

Running title: Membrane proteomics of Pi-starved *cnih5* root

Synopsis: *Arabidopsis thaliana* CORNICHON HOMOLOG 5 (*At*CNIH5) acts as a low phosphate (Pi)-responsive hub that controls efficient ER export of specific membrane cargoes beyond PHT1 Pi transporters to improve plant fitness under suboptimal Pi availability. Unlike the fungal and rice CNIHs interacting with their cognate cargoes through the C-terminal acidic motif, *At*CNIH5 employs a distinct cargo selection mechanism for *At*PHT1;1.

Key words: CORNICHON HOMOLOG, ER cargo receptor, coat protein complex II

32 (COPII), phosphate starvation, phosphate transporter, 4-hexylphenylazosulfonate (Azo)

Summary

- To find potential membrane cargoes of *Arabidopsis thaliana* CORNICHON HOMOLOG 5 (*At*CNIH5), a phosphate (Pi) deficiency-induced ER cargo receptor, we applied the UV-cleavable 4-hexylphenylazosulfonate (Azo)-solubilized microsomal protein extraction for iTRAQ-based proteomic analysis and identified 106 downregulated proteins in the Pi-limited roots of *cnih5*, including PHOSPHATE TRANSPORTER 1 proteins (PHT1s) and transmembrane enzymes responsible for the biosynthesis of very long-chain fatty acids and their derivative extracellular aliphatic compounds, and nucleotide sugar for cell walls.
- We confirmed the interaction of *At*CNIH5 with several downregulated transporters in *cnih5*, including *At*PHT1s, *At*OCT1, *At*URGT6, *At*DTX21, and *At*DTX35, using the yeast split-ubiquitin and the *in-planta* tripartite split-GFP assays.
- The C-terminal acidic residue of *At*CNIH5 is not required to interact with *At*PHT1;1, implying that *At*CNIH5 employs a distinct cargo selection mechanism for *At*PHT1;1.
- We showed the upregulation of *At*CNIH5 proteins in the Pi-limited root and in the Pi-replete root of the Pi overaccumulator *pho2*. As increasing *in-situ* *At*CNIH5 expression/activity enhances plant growth, we propose that *At*CNIH5 functions as a low Pi-responsive hub, facilitating the ER export of specific membrane cargoes and thereby improving plant fitness under suboptimal Pi availability and promoting agricultural sustainability.

57 **Introduction**

58 Phosphorus (P) is an essential macronutrient for plant growth and development
59 (Poirier & Bucher, 2002; Poirier *et al.*, 2022). Due to the low concentration of inorganic
60 phosphate (Pi) in soil—the primary form of P that plants absorb, applying Pi fertilizer has
61 become a common practice to improve crop productivity. However, the limited mobility
62 of Pi in soil prevents plants from acquiring most applied Pi fertilizer, leading to P runoff
63 into aquatic ecosystems. Therefore, developing plants with increased Pi uptake and high-
64 use efficiency is critical to minimizing the usage of Pi fertilizer, thus reducing
65 environmental pollution and achieving agricultural sustainability.

66 To adapt to the low Pi bioavailability, plants have many strategies to enhance external
67 Pi acquisition and internal Pi remobilization, which involve different Pi transporters at
68 distinct subcellular compartments. *PHOSPHATE TRANSPORTER 1* (*PHT1*) genes
69 encode the plasma membrane (PM)-localized Pi transporters responsible for the uptake
70 and the intercellular translocation of Pi. Even though Pi deprivation upregulates most
71 *PHT1* genes at the transcript level, the biosynthesis, secretion, and recycling rate of PHT1
72 proteins (PHT1s) also determine their abundance at the PM (Nussaume *et al.*, 2011).
73 Multiple post-translational mechanisms have been elucidated to regulate the protein
74 expression and the PM localization of PHT1s. The plant-specific SEC12-related
75 PHOSPHATE TRANSPORTER TRAFFIC FACILITATOR1 (PHF1) contributes to the
76 accumulation of PHT1s at the PM by assisting the PHT1s transit through the endoplasmic
77 reticulum (ER) (González *et al.*, 2005; Bayle *et al.*, 2011; Chen *et al.*, 2015). The rice
78 casein kinase II (CK2) diminishes the interaction between *Os*PT8 and *Os*PHF1 by
79 phosphorylating *Os*PT8, resulting in the ER retention of *Os*PTs (Chen *et al.*, 2015). On
80 the contrary, the protein phosphatase type 2C *Os*PP95 acts antagonistically with *Os*CK2
81 (Yang *et al.*, 2020). In addition, under Pi sufficiency, the ubiquitin-conjugating E2
82 enzyme UBC24/PHOSPHATE2 (PHO2) at the ER or post-ER compartments mediates
83 the ubiquitination of the endomembrane-associated *At*PHT1s followed by the vacuolar
84 degradation (Huang *et al.*, 2013). The PM-localized ubiquitin E3 ligase NITROGEN
85 LIMITATION ADAPTATION (NLA) participates in the ubiquitination-mediated and
86 clathrin-dependent endocytosis of PHT1s when Pi is replete (Lin *et al.*, 2013; Park *et al.*,
87 2014).

88 The ER is the start site where newly synthesized PHT1s travel towards the PM. The

ER-to-Golgi transport of PHT1s relies on the coat protein complex II (COPII)-mediated vesicles or carriers (Bayle *et al.*, 2011). However, how diverse membrane cargoes associated with Pi starvation are transported in the late secretory pathway and whether post-translational modification events regulate packaging of these cargoes into COPII vesicles remains largely unknown. The formation of COPII vesicles is a multi-step process that involves the recruitment of five core cytosolic factors, SAR1, SEC23, SEC24, SEC13, and SEC31, to the ER exit sites (ERES) (Barlowe and Miller, 2013; Kurokawa and Nakano, 2018). In particular, incorporation of multi-spanning transmembrane (TM) proteins into COPII vesicles in the budding yeast *Saccharomyces cerevisiae* requires dual interaction with the COPII coat subunit Sec24 and the ER cargo receptor Erv14 (Powers and Barlowe, 1998; Harmel et al., 2012; Pagant et al., 2015). The function of Erv14 in COPII coupling was presumably mediated by its role as a membrane chaperone that exposes sorting signals of Erv14 clients to interact with Sec24 for efficient capture into COPII vesicles (Dancourt and Barlowe, 2010; Pagant et al., 2015). Loss of the fungal Erv14 compromised the targeting of several transporters destined for the late secretory compartments, thus misregulating numerous cellular functions (Powers and Barlowe, 1998; Nakanishi et al., 2007; Pagant et al., 2015; Zimmermannová et al., 2019; Zheng et al., 2023). The *Drosophila* Cornichon (Cni), like its yeast homolog Erv14, was shown to recruit the epidermal growth factor (EGF)-like ligand Gurken into COPII vesicles (Roth *et al.*, 1995; Bökel *et al.*, 2006). Without Cni, the ER export and secretion of Gurken are disrupted (Bökel *et al.*, 2006). Similarly, the plant CNIHs act as the ER cargo receptors for various ion and metabolite transporters (Rosas-Santiago *et al.*, 2015; Wudick *et al.*, 2018; Wei *et al.*, 2023; Yáñez-Domínguez *et al.*, 2023).

Our recent side-by-side study uncovered that *Arabidopsis thaliana CORNICHON HOMOLOG 5* (*AtCNIH5*) is a Pi starvation-induced (PSI) gene and preferentially expressed in the outer layers of the root above the apical meristem (Chiu *et al.*, 2024). *At*CNIH5 localizes to the ER and is closely associated with the *At*SAR1A/*At*SEC16A/*At*SEC24A-labeled ERES (Chiu *et al.*, 2024). The *cnih5* mutant exhibited a lower abundance of *At*PHT1s in the root microsomal fractions, with reduced shoot Pi levels and shoot-to-root distribution of Pi under Pi sufficiency and decreased Pi uptake under Pi deficiency (Chiu *et al.*, 2024). In the Pi-limited root of *cnih5*, the fluorescent protein tagged-*At*PHT1;1 was in part retained intracellularly in the epidermis

121 within the transition/elongation zones and in the root hair (Chiu *et al.*, 2024).
122 Consistently, the fluorescence intensities of *At*PHT1;1 fusion proteins at the PM of the
123 root cells mentioned above also diminished in the Pi-limited *cnih5* relative to the wild-
124 type (WT) control (Chiu *et al.*, 2024), supporting a potential role for *At*CNIH5 in the
125 efficient transport of *At*PHT1s from the ER to the Golgi. Additional phenotypes, such as
126 shorter root hair length and increased root hair and lateral root densities, were also
127 observed for *cnih5* under Pi deficiency (Chiu *et al.*, 2024). Considering that *At*CNIH5
128 may serve as a cargo receptor for a broader range of membrane proteins and that
129 inefficient ER export of cargoes in *cnih5* can cause their intracellular retention and
130 eventual degradation due to the protein quality control, we inferred that the pleiotropy of
131 *cnih5* is likely consequences of mistargeting and/or downregulation of membrane cargoes
132 of *At*CNIH5 beyond *At*PHT1s.

133 To identify potential cargoes of *At*CNIH5 associated with Pi starvation, we employed
134 isobaric tags for relative and absolute quantification (iTRAQ)-based membrane
135 proteomics. Because membrane proteins are highly hydrophobic and have low
136 abundance, isolation of microsomal proteins (MPs) enriched for PM, ER, Golgi, vacuolar
137 membranes, and endosomal vesicles is challenging (Wang & Liang, 2012).
138 Conventionally, MPs are solubilized with sodium dodecyl sulfate (SDS) or other anionic
139 detergents. However, SDS impacts the liquid chromatography-tandem mass spectrometry
140 (LC–MS/MS) performance, and the removal step of SDS before mass spectrometry
141 analysis leads to an inevitable loss of MPs (Wang & Liang, 2012). A study using the rice
142 leaf as a model system demonstrated that the microcentrifugation-based microsomal
143 protein extraction (MME) method is effective for the downstream label-free quantitative
144 proteome analysis, requiring neither a large amount of plant material nor a step of
145 ultracentrifugation to enrich the PM proteins (Nguyen *et al.*, 2021). The authors also
146 applied the UV-cleavable and mass spectrometry-compatible surfactant, 4-
147 hexylphenylazosulfonate (Azo) (Brown *et al.*, 2019; Brown *et al.*, 2020), to avoid protein
148 losses by omitting the SDS detergent wash step. Their results revealed several advantages
149 of Azo over SDS in solubilizing the MPs, including a higher number and abundance of
150 MPs (Nguyen *et al.*, 2021). In this study, we modified the Azo-solubilized MME method
151 and isolated the root MPs from Pi-limited *Arabidopsis* WT and *cnih5* for iTRAQ-based
152 proteomic analysis. We targeted our research to root MPs to reduce sample complexity,

153 thus increasing the possibility of identifying functionally relevant protein changes in
154 *cnih5*. In addition, the membrane proteome analysis of Pi-limited roots is valuable in
155 gaining insight into the physiological role of *At*CNIH5. It also provides the first database
156 of the membrane proteome for Pi-limited root biology research (Zhou *et al.*, 2022).
157 With this approach, we identified 4,317 proteins in the Pi-limited WT and *cnih5* roots,
158 in which 1231 proteins (28.5%) have at least one TM helix. Of the differentially expressed
159 proteins (DEPs) in *cnih5*, 372 and 106 proteins are upregulated and downregulated by a
160 1.25-fold change, respectively, including the downregulation of *At*PHT1;1–1;5,
161 corroborating our recent finding that *At*PHT1s are genuine cargoes of *At*CNIH5 (Chiu *et*
162 *al.*, 2024). Consistent with the primary role of *At*CNIH5 in the ER export of membrane
163 cargoes, the enrichment analyses of Gene Ontology (GO) and Kyoto Encyclopedia of
164 Genes and Genomes (KEGG) pathways suggested a close association of the
165 downregulated proteins with protein export and localization. We also found that the
166 transmembrane enzymes involved in the biosynthesis of nucleotide sugar for cell walls,
167 very long-chain fatty acids (VLCFAs), and their derivative extracellular aliphatic
168 compounds, such as cutin, suberin, and wax, were downregulated in the Pi-limited roots
169 of *cnih5*.
170 We used the yeast split-ubiquitin system (SUS) and the *in-planta* tripartite split-GFP
171 assay to confirm the interaction of the potential membrane cargoes with *At*CNIH5,
172 including *At*PHT1s and several transporters. Our immunoblot results demonstrated the
173 induction of *At*CNIH5 in the Pi-limited root and the upregulation of *At*CNIH5 in the Pi-
174 replete root of the Pi overaccumulator *pho2*, likely as a result of accommodating the
175 increased demand for ER export of *At*PHT1s. We also generated a series of C-terminally
176 truncated forms of *At*CNIH5 to find out which motif of *At*CNIH5 interacts with
177 *At*PHT1;1. We showed that the C-terminal acidic residue, aspartic acid, is not required to
178 interact with *At*PHT1;1. Instead, *At*CNIH5 1–26, containing the first transmembrane
179 domains (TMD) alone, is sufficient to interact with *At*PHT1;1. Therefore, unlike the
180 fungal and rice CNIHs interacting with their cognate cargoes through the C-terminal
181 acidic motif (Rosas-Santiago *et al.*, 2017), *At*CNIH5 employs a distinct mechanism to
182 select *At*PHT1;1 as its cargo. Importantly, introducing the *At*CNIH5 genomic-GFP
183 translation fusion to complement the *cnih5* mutant boosted plant growth under suboptimal
184 Pi supply, revealing that *At*CNIH5 acts as a hub to facilitate the ER export of specific

185 membrane cargoes associated with Pi starvation to improve plant fitness.
186
187 **Materials and Methods**
188 **Plant Material and Growth Conditions**
189 Seeds of the *A. thaliana* wild-type (Columbia, Col-0) and *cnih5* (SAIL_256_B03)
190 mutants used in this study were obtained from the Arabidopsis Biological Resource
191 Center. Seeds were surface-sterilized and germinated on agar plates with one-half
192 modified Hoagland's solution containing 1% sucrose and 0.7% Bacto agar and grown in
193 the growth chamber at 22 °C with a 16-h light/8-h dark cycle. Pi-sufficient (+P; 250 μM
194 Pi) or Pi-deficient (−P; 0 μM Pi) medium containing 1.2% agar was used for vertically
195 grown plants.
196
197 **Tissue Homogenization and Microsomal Protein Preparation**
198 The roots of 11-day-old seedlings with five days of Pi starvation were harvested.
199 Approximately 100 mg of root tissue was collected for each sample and stored at −80 °C
200 for subsequent homogenization. The frozen samples were homogenized by TissueLyser
201 II (QIAGEN). The method for microsomal protein extraction was modified from a
202 previous study (Abas & Luschnig, 2010), and all steps were performed on ice or 4 °C.
203 Briefly, each sample was resuspended in 100 μl of extraction buffer (EB) containing 50
204 mM of hydroxyethyl piperazine ethane sulfonic acid (HEPES; Melford, pH 7.5), 25%
205 (w/w 0.81 M) sucrose, 5% (v/v) glycerol, 10 mM of ethylenediaminetetraacetic acid
206 (EDTA; Amresco, pH 8), 5 mM of KCl, 1 mM of dithiothreitol (DTT; Sigma), and 2×
207 protease inhibitor cocktail (P9599, Sigma). An equivalent volume (100 μl) of 5%
208 polyvinylpolypyrrolidone (PVPP; Sigma) suspension solution was used for each sample.
209 The 5% PVPP was centrifuged at 2,000×g for 1 min at room temperature (RT). The
210 precipitate was activated for 2 hours in an equivalent volume of activated solution
211 containing 100 mM HEPES, 40% (w/w, 1.37 M) sucrose, 20 mM EDTA, and 10 mM
212 KCl. The activated PVPP was centrifuged at 5,000×g for 1 min at RT, and the supernatant
213 was removed. The activated PVPP pellet was mixed with the sample suspension and stood
214 for 5 min, followed by centrifugation thrice. The first centrifugation was processed at
215 600×g for 3 min. The pellet was then re-extracted with 50 μl EB and centrifuged at 600×g
216 for 3 min. The pellet was then re-extracted with 35 μl EB and centrifuged at 2,000×g for

217 30 s. After three times centrifugation, all the supernatants were combined and centrifuged
218 again at 600×g for 3 min. The collected supernatant was diluted with an equivalent
219 volume of ddH_2O to reach a final solution concentration containing 12–13% sucrose and
220 centrifuged at 21,000×g for 90 min. The pellet was resuspended in washing buffer
221 containing 10 mM HEPES, 5 mM EDTA, 1 mM phenylmethylsulfonyl fluoride (PMSF,
222 Sigma), and 1× protease inhibitor cocktail and centrifuged at 21,000×g for 45 min. Finally,
223 the pellet was stored at −80 °C for further analysis.
224
225 **Protein Solubilization and In-Solution Digestion**
226 Microsomal protein pellets were dissolved in 1% sodium 4-hexylphenylazosulfonate (Na-
227 Azo, Excenen Pharmatech) in 100 mM triethylammonium bicarbonate (TEABC, Sigma)
228 containing 2× protease inhibitor cocktail and 1 mM PMSF. The protein yield was
229 determined by BCA assay (Pierce). For each sample, an equal amount of protein was
230 reduced with 5 mM tris-(2-carboxyethyl)-phosphine (TCEP, Sigma) at 60 °C for 30 min,
231 followed by cysteine-blocking with 10 mM methyl methanethiosulfonate (MMTS, Sigma)
232 at 25 °C for 30 min. Samples were digested with sequencing-grade modified porcine
233 trypsin (Promega) at 37 °C with shaking for 1 hour and then illuminated by 6W UV light
234 302 nm (UVP UVM-57, Analytik Jena) at 4 °C for 40 min. The digested proteins were
235 then aliquot and stored at −20 °C until use.
236
237 **Isobaric Tag for Relative and Absolute Quantitation (iTRAQ) Labeling and Peptide**
238 **Separation**
239 After trypsin digestion, 0.5 μg of peptides was subjected to 1D–LC–MS/MS without pre-
240 fractionations to identify and quantify proteins as a quality control study. On the other
241 hand, 10 μg of peptides was labeled using an iTRAQ Reagent-4 plex Multiplex Kit
242 according to the manufacturer's instructions (Applied Biosystems) for 1 hour at RT. Two
243 WT replicates were labeled with iTRAQ-114 and -115, and two *cnih5* replicates were
244 labeled with iTRAQ-116 and -117, pooled and desalted by homemade C18-microcolumn
245 (SOURCE 15RPC, GE Healthcare). The eluted peptides were dried by vacuum
246 centrifugation. The desalted peptides were loaded onto a homemade strong cation
247 exchange (SCX) column (Luna SCX 5μm, 0.5 × 120 mm) at a 2 μl/min flow rate for 60
248 min. The peptides were then fractionated to 24 fractions by eluting with 0 to 100% HPLC

249 buffer B (1 M ammonium nitrate/25% acetonitrile/0.1% formic acid) using on-line two-
250 dimensional high-performance liquid chromatography (2D-HPLC; Dionex Ultimate
251 3,000, Thermo Fisher). Each SCX fraction was diluted in-line before trapping onto a
252 reverse-phase (RP) column (Zorbax 300SB-C18, 0.3 x 5 mm; Agilent Technologies). The
253 peptides were then separated on a column (Waters BEH 1.7 μm, 100 μm I.D. × 10 cm
254 with a 15 μm tip) using a multi-step gradient of HPLC buffer C (99.9% acetonitrile/0.1%
255 formic acid) for 60 min with a flow rate of 0.3 μl/min.
256
257 **Liquid Chromatography-Tandem Mass Spectrometry (LC-MS/MS) Analysis**
258 The LC apparatus was coupled with a 2D linear ion trap mass spectrometer (LTQ-
259 Orbitrap ELITE; Thermo Fisher) operated using Xcalibur 2.2 software (Thermo Fisher).
260 The full-scan MS was performed in the Orbitrap over a range of 400 to 2,000 Da and a
261 resolution of 120,000 at m/z 400. For proteome analysis, the 10 data-dependent MS/MS
262 scan events (10 MS2 HCD) were followed by one MS scan for the 10 most abundant
263 precursor ions in the preview MS scan. The m/z values selected for MS/MS were
264 dynamically excluded for 80 sec with a relative mass window of 1 Da. The electrospray
265 voltage was set to 1.8 kV, and the capillary temperature was set to 200 °C. MS and MS2
266 automatic gain control were set at 1,000 ms (full scan) and 300 ms (MS2 for HCD), or 3
267 $\times 10^6$ ions (full scan) and 3×10^4 ions (MS2 for HCD) for maximum accumulated time
268 or ions.
269
270 **LC-MS Data Processing, Protein Identification and Quantification**
271 Proteome Discoverer software (version 2.3, Thermo Fisher Scientific) was used for data
272 analysis, incorporating the reporter ions quantifier node for iTRAQ quantification. The
273 MS/MS spectra were searched against the SwissProt database using the Mascot search
274 engine (Matrix Science, version 2.5). For peptide identification, a 10 ppm mass tolerance
275 was allowed for intact peptide masses and 0.2 Da for HCD fragment ions, with allowance
276 for two missed cleavages made from trypsin digestion. Variable modifications included
277 oxidized methionine, acetylation (protein N-terminal), and iTRAQ-4plex (peptide N-
278 terminal, K); methylthiolation (C) was considered a static modification. Peptide-spectrum
279 matches (PSMs) were filtered based on high confidence and Mascot search engine rank
280 1 of peptide identification, ensuring an overall false discovery rate (FDR) below 0.01.

281 Proteins with only a single peptide hit were removed. Quantitative protein data were
282 exported from Proteome Discoverer using Integration Methods of the Most Confident
283 Centroid with a 20 ppm tolerance. The data sets were analyzed by cross-comparison
284 between four samples (ratio 1, 116:114; ratio 2, 117:114; ratio 3, 116:115, and ratio 4,
285 117:115). Protein ratios in each comparison group were normalized using the median
286 ratio of each comparison group. Volcano plots of differentially expressed proteins were
287 generated using the ggplot2 (Wickham *et al.*, 2016) and ggrepel (Slowikowski *et al.*, 2024)
288 package in R version 4.3.1 (R Core Team, 2021). The code was written using RStudio
289 version 2023.06.2 (RStudio Team, 2020). A 1.25-fold cutoff was applied to define
290 differentially expressed proteins in each comparison group.
291
292 **Protein Annotation and Interpretation**
293 Transmembrane-related information was obtained through analysis using DeepTMHMM
294 (https://dtu.biolib.com/DeepTMHMM) (Hallgren *et al.*, 2022). Subcellular structure
295 localization was analyzed by SUBA5 (https://suba.live/) (Hooper *et al.*, 2016). For
296 functional annotation of proteins, Gene Ontology (GO) and Kyoto Encyclopedia of Genes
297 and Genomes (KEGG) enrichment analyses were determined by ShinyGO 0.80
298 (http://bioinformatics.sdstate.edu/go/) (Ge *et al.*, 2019), in which *p*-values were computed
299 using the hypergeometric test and multiple test correction was performed using the
300 Benjamini–Hochberg method based on an FDR cut-off of 0.05. Only pathways with a
301 minimum of 10 genes were selected. Similar pathways that share 95% of their genes and
302 50% of the words in their names were eliminated according to the setting of ShinyGO
303 0.80. Dot plots of GO enrichment analysis were generated using the ggplot2 (Wickham
304 *et al.*, 2016) and stringr package (Wickham, 2023).
305
306 **Microsomal protein extraction for immunoblot analysis**
307 The MPs pellets were solubilized by 0.5% Azo in 25mM aqueous ammonium
308 bicarbonate, pH 7.0 (919233; Sigma Aldrich). Alternatively, the low-speed pellet (LSP)
309 was prepared as previously described (Yoshimoto *et al.*, 2004), and microsomal protein
310 was isolated using the Minute Plant Microsomal Membrane Extraction Kit (Invent, MM-
311 018) according to the manual instructions. A 15–30 μg of MPs from each sample was
312 loaded onto 4–12% Q-PAGE™ Bis-Tris Precast Gel (SMOBIO) or NuPAGE 4–12% Bis-

313 Tris Gels (Thermo Fisher Scientific). Gel was transferred to polyvinylidene difluoride
314 membranes (IPVH00010 Immobilon-P Membrane or ISEQ00010 Immobilon®-PSQ
315 Membrane; Merck). Membrane was blocked with 1–2% BSA in 1× PBS solution with
316 0.2% Tween 20 (PBST, pH 7.2) at RT for 1 h, and rinsed two times with distilled water
317 followed by hybridization with primary antibodies of *At*PHF1 (Huang *et al.*, 2013),
318 *At*PHO1 (Liu *et al.*, 2012), *At*NRT2.1 (AS12 2612; Agrisera), and *At*CNIH5 at RT for 2
319 h or at 4 °C overnight in blocking solution. Polyclonal rabbit *At*CNIH5 antibody was
320 raised against the region corresponding to the amino acid residues 96 to 114
321 (TELYNTNKWEQKKRVYKIG) by LTK BioLaboratories, Taiwan, and was affinity
322 purified. The membrane was washed four times with 1× PBST for 5 min followed by
323 hybridization with the horseradish peroxidase–conjugated secondary antibody
324 (GTX213110-01 or GTX213111-01; GeneTex) in blocking solution at RT for 1 h. After
325 four washes in 1× PBST for 5 min and a rinse with distilled water, chemiluminescent
326 substrates (WesternBright ECL or Sirius; Advansta) were applied for signal detection.
327
328 **Construct design and yeast split-ubiquitin assay**
329 For constructing the yeast expression clones, the coding sequence (CDS) of the gene of
330 interest (GOI), including *At*LRK10L-1.1, *At*GXM2, *At*SOS, *At*DTX21, *At*DTX35,
331 *At*URGT6, *At*OCT1, *At*SEC24A, *At*SEC24B, *At*SEC24C and the truncated *At*CNIH5
332 variants, was amplified by PCR, cloned into the pCR8/GW/TOPO vectors and sequenced.
333 The pCR8/GW/TOPO construct containing the CDS of *AtPHT1;1* was cloned as
334 previously reported (Huang *et al.*, 2013). The entry clones were recombined into
335 NX32_GW (ABRC CD3-1737) or XN22_GW (ABRC CD3-1735) through LR reactions,
336 resulting in N or C-terminally fused Nub fragments or into MetYC_GW (ABRC CD3-
337 1740) through LR reactions, resulting in *At*PHT1;1-PLVCub. The PLVCub-*At*CNIH5
338 construct was generated as recently reported (Chiu *et al.*, 2024). The Nub and PLVCub
339 expression clones were sequentially transformed into the yeast THY.AP4 strain (ABRC
340 CD3-808; (Obrdlik *et al.*, 2004). Fresh yeast colonies picked from yeast extract peptone
341 dextrose adenine (YPDA) medium or synthetic complete (SC) medium without leucine
342 (SC–L) were inoculated in the corresponding liquid medium and incubated overnight at
343 30 °C with shaking at 200 rpm. Overnight yeast culture was then diluted to OD_{600} = 0.2
344 and grew for another 4–6 h until OD_{600} reached 0.4–0.6. Yeast pellet was collected by

345 centrifugation at 2,000×g at 4 °C for 10 min, washed with ddH_2O, and resuspended in
346 Tris-EDTA/lithium acetate solution (TE/LiAc, 10 mM Tris-HCl [pH 8.0], 1 mM EDTA,
347 and 0.1 M lithium acetate). Yeast transformants carrying the PLVCub-*At*CNIH5 or
348 *At*PHT1;1-PLVCub were selected and maintained on SC–L for sequential transformation
349 with NubI (positive control), NubG (negative control), and GOI-NubG or NubG-GOI.
350 Yeast transformants carrying the Nub and the PLVCub constructs were selected and
351 maintained on SC medium without leucine and tryptophan (SC–LW). For the protein–
352 protein interaction testing, yeast cells co-expressing PLVCub-*At*CNIH5 or *At*PHT1;1-
353 CubPLV with GOI-NubG or NubG-GOI were grown on synthetic media lacking leucine,
354 tryptophan, adenine, and histidine (SC–LWAH) with 500 μM methionine or on SC–LW
355 containing 100 mg/L 5-bromo-4-chloro-3-indolyl-*β*-d-galactopyranoside (X-Gal) at 30
356 °C for 24–36 h. Primer sequences used are listed in Supporting Information Table S4.
357
358 **Construct design for split-GFP assays in *N. benthamiana* leaves and *Arabidopsis***
359 **transgenic plants**
360 The *UBQ10:sXVE:* S10-*At*CNIH5 clone was obtained as recently reported (Chiu *et al.*,
361 2024). For the transient expression of *At*PHT1;1-S11, *At*SOS-S11, *At*DTX21-S11,
362 *At*DTX35-S11, *At*URGT6-S11, *At*OCT1-S11, *At*HAK5-S11, *At*VPE1-S11 and
363 *At*SULTR1;3-S11, the CDS or the corresponding fragment was amplified by PCR and
364 subcloned into *UBQ10:sXVE*: (MCS)-S11 (Addgene plasmid # 108179). For subcellular
365 localization analysis of the protein of interest, either *UBQ10:sXVE:* S11-GFP1–9
366 (Addgene plasmid # 125665) or *UBQ10:sXVE:* GFP1–10 (Addgene plasmid # 125663)
367 was co-expressed. For the tripartite split-GFP reconstitution, the constructs encoding
368 S10-tagged and S11-tagged protein fusions were co-expressed in the presence of
369 *UBQ10:sXVE*: GFP1–9 (Addgene plasmid # 108187). Co-expression with 3xHA-S11
370 (Addgene plasmid # 108238) was used as a negative control for protein–protein
371 interaction. The brightness of the images for the protein–protein interaction was adjusted
372 by a 20% increase and the contrast adjusted by a 20% decrease. Primer sequences used
373 are listed in Supporting Information Table S1. For the genomic GFP-*AtCNIH5*
374 complemented plants (*AtCNIH5pro*: GFP-*AtCNIH5/cnih5*), the construct design was
375 recently described (Chiu *et al.*, 2024).
376

377 ***Agrobacterium tumefaciens*-mediated infiltration of *N. benthamiana* leaves**
378 *Agrobacterium tumefaciens* strain EHA105 harboring the expression constructs or p19
379 was cultured in Luria–Bertani (LB) medium with the appropriate antibiotics [gentamicin
380 (50 μg ml^{-1}), rifampicin (5 μg ml^{-1}) or kanamycin (50 μg ml^{-1})]. Cells were resuspended
381 in the infiltration medium containing 10 mM $MgCl_2$, 10 mM MES (pH 7.5), and 150 μM
382 acetosyringone, and co-infiltrated to the true leaves of 3–5-week-old tobacco plants. For
383 the *β*-estradiol-inducible split-GFP system, 36.7 μM *β*-estradiol was applied as previously
384 described (Liu *et al.*, 2018; Liu, 2021). Infiltrated leaves were collected 2 days post-
385 infiltration (dpi) for confocal imaging.
386
387 **Confocal microscopy**
388 Confocal microscopy images were acquired using Zeiss LSM 800 (Zeiss) with objectives
389 Plan-Apochromat 10×/0.45 M27, 20×/0.8 M27, and 40×/1.3 Oil DIC M27 in multi-track
390 mode with line switching and averaging of two reading. Excitation/emission wavelengths
391 were 488 nm/410–546 nm for GFP and 561 nm/656–700 nm for RFP and mCherry.
392
393 **Chemical treatments**
394 Acetosyringone (150 mM stock in DMSO; D134406; Sigma-Aldrich) was diluted to a
395 final concentration of 150 μM in ddH_2O. *β*-estradiol (36.7 mM stock in ethanol; E2758;
396 Sigma-Aldrich) was diluted to a final concentration of 36.7 μM in ddH_2O. For monitoring
397 the degradation of 1% Azo following the UV irradiation, 1% sodium 4-
398 hexylphenylazosulfonate (Na-Azo, Excenen Pharmatech) in 100 mM TEABC buffer was
399 1: 200 diluted and subjected to absorbance measurement.
400
401 **Results**
402 **Azo-solubilized microcentrifugation-based microsomal protein extraction (MME)**
403 **of *Arabidopsis* roots**
404 Because the application of Azo promoted fast and reproducible tryptic digestion for
405 quantitative proteomics (Brown *et al.*, 2020), we replaced the mass spectrometry-
406 incompatible surfactant SDS with Azo and established an efficient workflow of MPs
407 extraction for quantitative proteomic analysis of *Arabidopsis* roots (Fig. **1a**). To ensure
408 that the Azo wash step can be skipped prior to mass spectrometry analysis, we tested the

409 time-course effect of UV irradiation on Azo breakdown (Brown *et al.*, 2019). Within 40
410 min of UV illumination, 1% Azo in 100 mM triethylammonium bicarbonate (TEABC)
411 almost wholly degraded (Fig. **1b**). After tryptic digestion and Azo degradation, small
412 aliquots of four samples—two biological replicates each for WT and *cnih5*, were pre-
413 analyzed in a single one-dimensional (1D)–LC–MS/MS run. Summary of the label-free
414 proteomic analysis was shown in Supporting Information Fig. S1a. We used multiple
415 marker abundance profiling (MMAP) (Hooper *et al.*, 2016) to estimate the relative
416 organelle abundance in the MPs samples. The results suggested that the modified Azo-
417 solubilized MME method greatly removed proteins targeted to the plastid, nucleus, and
418 extracellular space while enriching proteins targeted to the mitochondria, ER, Golgi, PM,
419 and vacuole (Supporting Information Fig. S1b, Fig. S1c). To further evaluate this
420 modified method, we examined by immunoblot the expression of the well-established
421 root MPs, including the ER-resident *At*PHF1, the Golgi-localized *At*PHO1 (Arpat *et al.*,
422 2012; Liu *et al.*, 2012), and the PM-targeted *At*PHT1;1/2/3 and *At*NRT2.1 (Chopin *et al.*,
423 2007). As previously reported, *At*PHF1, *At*PHO1, and *At*PHT1;1/2/3 were upregulated
424 following Pi deprivation (Fig. **2a**). Interestingly, regardless of Pi availability, the protein
425 amounts of *At*PHF1 and *At*PHO1 were more abundant in *cnih5* than in WT, while
426 *At*PHT1;1/2/3 was downregulated in *cnih5* compared to the WT controls (Fig. **2a**).
427 *At*NRT2.1 expression declined by Pi starvation and showed no differences between WT
428 and *cnih5* (Fig. **2a**). Collectively, these results justified the suitability of our modified
429 Azo-solubilized MME method for enriching root MPs.
430
431 **Upregulation of *At*CNIH5 in the root of the Pi overaccumulator *pho2***
432 As we attempted to determine the expression of *At*CNIH5 in the root MPs, a specific
433 polyclonal antibody against *At*CNIH5 was raised. This antibody recognized a band in the
434 WT at ∼15 kDa that was absent in *cnih5* (Fig. **2b**). In agreement with the finding that low
435 Pi induces the gene expression of *AtCNIH5*, the protein amount of *At*CNIH5 was also
436 elevated in the Pi-limited root (Fig. **2b**), suggesting that *AtCNIH5* is upregulated by Pi
437 starvation at the transcript and protein level. Of note, under Pi sufficiency, *At*CNIH5 was
438 modestly increased in the root of the Pi overaccumulator *pho2* relative to the WT control
439 (Fig. **2b**), which was in line with the previous membrane proteomics data showing that
440 *At*CNIH5 significantly increased in the Pi-replete root of the overaccumulator *pho2*

441 relative to the WT (Huang *et al.*, 2013). The increase of *At*CNIH5 in the root of *pho2*
442 under Pi-sufficient conditions was also recapitulated by two other different MPs
443 extraction methods (Fig. **2b**). Taken together, these results suggested that *At*CNIH5 is
444 induced by Pi starvation to meet the increased demand for ER export of *At*PHT1s, which
445 is substantiated by our genetic evidence that loss of *AtCNIH5* alleviates the Pi toxicity of
446 *pho2* (Chiu *et al.*, 2024).
447
448 **Quantitative membrane proteomic analysis of MPs in *Arabidopsis cnih5* roots under**
449 **Pi limitation**
450 Next, the peptides obtained after tryptic digestion were labeled with iTRAQ reagents,
451 combined, and separated by two-dimensional high-performance liquid chromatography
452 (2D–HPLC) into 24 fractions. Each fraction was diluted and trapped onto a reverse-phase
453 column for separation, followed by Orbitrap mass spectrometry. By combining the total
454 proteins of the four samples, we identified 32,812 peptides and 21,433 unique peptides
455 that matched with 4,317 proteins with confidence (criteria described in Material and
456 Method), resulting in an average sequence coverage of 17.8% (Supporting Information
457 Table S2). About 99.3% of the identified proteins were shared across the four samples
458 (Supporting Information Table S2), indicating that our proteomic data were unbiased, as
459 nearly all proteins within the detection range could be identified. The proteins containing
460 TM helices were predicted or annotated by DeepTMHMM and UniProtKB (Fig. **3a)**
461 (Krogh *et al.*, 2001; Hallgren *et al.*, 2022; The UniProt Consortium, 2023). 1231
462 identified proteins (28.5%) have at least one TM helix and are thus integral membrane or
463 TM proteins (Fig. **3a**). We classified the subcellular localizations of the 4,317 identified
464 proteins using SUBA5 (Hooper *et al.*, 2016), showing 7.8% of the identified proteins
465 localized to the ER, 10.1% to the Golgi, 4.4% to the vacuole, and 16.2% to the PM (Fig.
466 **3b**). About 37.3% (1609) and 21.2% (915) of the identified proteins represent MPs and
467 integral MPs, respectively (Fig. **3a**). In contrast, 19.3% of the 1231 TM proteins localized
468 to the ER, 15.7% to the Golgi, 9.7% to the vacuole, and 31.7% to the PM (Fig. **3c**). The
469 general and detailed descriptions of proteomics data, including the summary of proteomic
470 analysis, protein scores and mass, annotation, and quantification for the identified
471 proteins, are listed in Supporting Information Table S2. The 4,317 identified proteins
472 were subjected to GO enrichment analysis by Shiny GO 0.80 (Ge *et al.*, 2019). Only the

473 top significant GO terms (FDR adj. p-value < 0.05) were shown according to the ranking
474 of fold enrichment. In the molecular function (MF) category, the top terms are nucleoside-
475 triphosphatase (NTPase) activity, pyrophosphatase (PPase) activity, and mRNA binding;
476 in the biological process (BP) category, the top terms are intracellular transport, protein
477 transport, and establishment of protein localization; in the cellular component (CC)
478 category, plant-type vacuole, cell-cell junction, and plasmodesmata are enriched
479 (Supporting Information Fig. S2, Table S2), indicating that Pi depletion impacts NTP-
480 and PPi-dependent cellular events required for the endomembrane trafficking.

481 In comparison to the previous study by Lan et al. (Lan *et al.*, 2012), which examined
482 quantitative total protein profiling in Pi-deficient versus Pi-sufficient *Arabidopsis* roots,
483 we found that among 209 significantly up-regulated proteins in their datasets (Pi-
484 deficient/Pi-sufficient plants ratio of ≥ 1.29), 57 proteins (including 13 integral MPs)
485 overlapped with the 4,317 proteins we identified from the Pi-limited roots (Supporting
486 Information Table S2**)**. Although this overlap accounts for approximately 27.3% of the
487 PSI proteins reported in their research, we identified an additional 902 integral MPs,
488 emphasizing that enriching MPs for proteomics could greatly expand the inventory of
489 identified proteins implicated in Pi starvation responses (Supporting Information Table
490 S2).

491 As anticipated, several *At*PHT1 members were downregulated in the Pi-limited root of
492 *cnih5* versus WT (Table **1**). Specifically, downregulation of *At*PHT1;2, *At*PHT1;3, or
493 *At*PHT1;4 was observed in at least three ratios (fold changes), with at least one ratio
494 showing FDR adj. p-value ≤ 0.05. While not statistically significant, the downregulation
495 of *At*PHT1;1 and *At*PHT1;5, along with the upregulation of *At*PHF1, displayed a
496 consistent trend across four ratios. In contrast, *At*PHT1;9 was upregulated in the Pi-
497 limited root of *cnih5* (Table **1**). These proteomic data were closely correlated with our
498 immunoblot results for *At*PHT1;1/2/3, *At*PHT1;4, and *At*PHF1 in the Pi-limited roots of
499 *cnih5* (Fig. **2a**), confirming the reliability of our quantitative proteomic analysis.

500 Volcano plots summarized the results from the four comparison groups, highlighting
501 the differentially expressed *At*PHT1 members and *At*PHF1 in green (**Fig. 3d**). Due to the
502 variability in the ratios of quantified *At*PHT1s across two biological replicates, we
503 increased the stringency of our protein profile comparisons. We defined DEPs as those
504 with at least two ratios ≥ 1.25 or ≤ 0.75, without applying FDR adjusted p-value cutoffs,

505 and excluded candidates showing any opposite trends (≥ 1.25 or ≤ 0.75). As a result, we
506 identified 372 proteins that were upregulated and 106 proteins that were downregulated
507 in *cnih5* (Supporting Information Table S3).

508 The 372 upregulated proteins in the Pi-limited roots of *cnih5* were subjected to the
509 enrichment analysis of GO and KEGG pathways (FDR adj. p-value < 0.05). In the MF
510 category, the top terms include copper ion binding, antioxidant activity, and
511 oxidoreductase activity acting on the CH–OH group of donors NAD or NA; in the BP
512 category, the top terms are sulfur compound biosynthetic process, purine nucleotide
513 metabolic process, and purine-containing compound metabolic process; in the CC
514 category, polysomal ribosome, polysome, and cytosolic ribosome are enriched
515 (Supporting Information Fig. S3a, Table S3), likely reflecting compensation mechanisms
516 for loss of *At*CNIH5. In particular, when we focused on the 51 upregulated integral MPs
517 and subjected them to the GO enrichment analyses, we discovered significant
518 associations with transporter activities (Supporting Information Fig. S3b). The KEGG
519 pathway enrichment analyses of the 372 upregulated proteins identified the most relevant
520 pathways related to ascorbate and aldarate metabolism, sulfur metabolism, and fructose
521 and mannose metabolism (Supporting Information Fig. S3c). This suggests that the
522 upregulated proteins in the Pi-limited *cnih5* roots are associated with carbohydrate
523 metabolic pathways that help protect cells against oxidative stress. Additionally, the
524 KEGG analyses of the 51 upregulated integral MPs revealed interactions related to
525 SNARE-mediated vesicular transport (Supporting Information Fig. S3d). Overall, the
526 dysfunction of *At*CNIH5 leads to alterations in vesicular trafficking.

527 In the GO enrichment analysis of the 106 downregulated proteins, the most significant
528 terms within the MF category include 7S RNA binding, fatty acid elongase activity,
529 structural constituent of chromatin, and transporter activity; for the BP categories, the top
530 terms are protein transport, cellular macromolecule localization, and establishment of
531 protein localization; in the CC categories, the enriched terms are the AP-type membrane
532 coat adaptor complex, membrane coat, coated membrane, and cytoplasmic vesicle
533 membrane (Fig. **4a** and Supporting Information Table S3). These results can be attributed
534 to the downregulation of proteins involved in the Golgi-associated clathrin assembly and
535 the signal recognition particle (SRP) subunits that mediate co-translational membrane
536 protein targeting (Supporting Information Table S3). We thus surmised that the loss of

537 *At*CNIH5 leads to negative feedback regulation on post-Golgi membrane trafficking,
538 which reduces the futile coated-vesicle assembly, and on protein synthesis to prevent the
539 toxic accumulation of *At*CNIH5-dependent cargoes in the ER. The enriched KEGG
540 pathways also include fatty acid elongation, protein export, cutin, suberin, and wax
541 biosynthesis, and biosynthesis of nucleotide sugars (Fig. **4b**). Overall, the downregulated
542 proteins in the Pi-limited root of *cnih5* are associated with protein export and localization,
543 acyl-lipid metabolism, and nucleotide sugar biosynthesis.
544

545 **Analysis of protein–protein interaction between *At*CNIH5 and its potential**
546 **membrane cargoes**

547 Assuming that potential cargoes of *At*CNIH5 are downregulated integral MPs in *cnih5*,
548 we narrowed the number of candidates to 31 (Table **2**). This list is over-represented with
549 three hypersensitive response-like lesion-inducing protein (HRLI)-like proteins
550 (AT3G23175, AT3G23190, and AT4G14420), two *β*-ketoacyl-CoA synthases (*At*KCS2
551 and *At*KCS20), and two *At*PHT1 members (*At*PHT1;1 and *At*PHT1;3) (Table **2**).
552 Although *At*HRLI-like proteins have not been characterized, the *N. benthamiana*
553 *Nb*HRLI4 conferred salicylic acid-mediated resistance to turnip mosaic virus (TuMV)
554 (Wu *et al.*, 2021). *AtKCS* genes encode 3-ketoacyl CoA synthases catalyzing the rate-
555 limiting condensation step of VLCFAs biosynthesis (Evenson & Post-Beittenmiller,
556 1995). *AtKCS2* and *AtKCS20* are highly expressed in the root endodermis and redundant
557 in root suberin biosynthesis (Lee *et al.*, 2009). Interestingly, two alcohol-forming fatty
558 acyl-CoA reductases, *At*FAR3/CER4 and *At*FAR5, are also downregulated and over-
559 represented in the KEGG pathway of cutin, suberin and wax biosynthesis (Fig. **4b** and
560 Supporting Information Table S3), suggesting that biosynthesis of VLCFAs and their
561 derivative extracellular aliphatic compounds are misregulated in the Pi-limited roots of
562 *cnih5*. Nevertheless, since *At*HRLI-like proteins and *At*KCS are ER-localized integral
563 MPs, the downregulation of these proteins may be a secondary effect due to the
564 impairment of *At*CNIH5.

565 We then selected a subset of the potential membrane cargoes (highlighted in gray in
566 Table **2**) to test their interaction with *At*CNIH5 based on the two criteria: (1) a TM protein
567 located in post-ER compartments of the secretory pathway and (2) having four ratios ≤
568 0.75 or at least two ratios ≤ 0.75 with at least one ratio showing FDR adj. *p*-value ≤ 0.05.

569 With the yeast SUS, the nutrient selection and LacZ β-galactosidase assays suggested that
570 besides *At*PHT1;1 and *At*PHT1;4 (Chiu *et al.*, 2024), *At*CNIH5 interacted with *At*PHT1;2,
571 *At*PHT1;5, *At*PHT1;7 and *At*PHT1;9 (Fig. **5a**), suggesting that *At*CNIH5 recognizes
572 conserved motifs among several *At*PHT1 members. We also confirmed the interaction of
573 *At*CNIH5 with the PM-localized receptor-like kinase *At*LRK10L-1.1 (AT1G18390),
574 nucleotide exchange factor *At*SOS (AT1G26650), and organic cation/carnitine
575 transporter *At*OCT1 (AT1G73220), the Golgi-localized nucleotide sugar transporters
576 *At*URGT6 (AT1G34020) and glucuronoxylan 4-O-methyltransferase *At*GXM2
577 (AT4G09990), and the tonoplast (TP)-localized detoxification efflux carriers *At*DTX21
578 (AT1G33110) and *At*DTX35 (AT4G25640) (Fig. **5b)**. We obtained similar results when
579 the expression constructs for *At*SOS, *At*OCT1 *At*URGT6, *At*DTX21, and *At*DTX35 were
580 generated with different fusion orientations (Supporting Information Fig. S4). *AtOCT1* is
581 a PSI gene (Liu *et al.*, 2016). Its expression is restricted to the vasculature of the root and
582 at sites of lateral root formation (Lelandais-Brière *et al.*, 2007). Therefore, the interaction
583 of *At*CNIH5 and *At*OCT1 is likely to occur in the vascular tissues. *At*URGT6 and
584 *At*GXM2 are cell wall-modifying enzymes. *At*URGT6 is involved in the biosynthesis of
585 rhamnogalacturonan-I (RG-I), a component of pectin found in mucilage and various types
586 of plant cell walls (Saez-Aguayo *et al.*, 2020). *At*GXM2 is a methyltransferase that
587 catalyzes 4-O-methylation of glucuronic acid (GlcA) side chains present on the
588 hemicellulose xylan (Lee *et al.*, 2012; Urbanowicz *et al.*, 2012; Yuan *et al.*, 2014).
589 *AtGXM2* is upregulated in response to Pi starvation (Liu *et al.*, 2016) and preferentially
590 expressed in the root hair (Salazar-Henao & Schmidt, 2016). *At*DTX21 and *At*DTX35
591 belong to the multidrug and toxic compound extrusion (MATE)-type transporter
592 superfamily. *At*DTX35 is also low Pi-responsive (Liu *et al.*, 2016) and functions as a
593 turgor-regulating chloride channel associated with root hair elongation (Zhang *et al.*,
594 2017). Defective *At*CNIH5 may modulate cell wall elasticity and root hair growth under
595 Pi limitation.

596 To explore other potential membrane cargoes of *At*CNIH5 that may be missing in our
597 iTRAQ-based proteomic data, we set out in parallel to find root PSI genes encoding
598 transporters that are co-regulated with *AtCNIH5*. We queried the RNA-seq dataset from
599 *Arabidopsis* seedlings subjected to Pi deprivation (P0: Pi-sufficiency; P1: one day of Pi
600 deprivation; P3: three days of Pi deprivation) (Liu *et al.*, 2016). Genes with expression

601 levels less than 1 RPKM were excluded. We filtered root PSI genes that displayed an
602 expression pattern similar to that of *AtCNIH5* based on (1) the $\log_2$FC ≥ 0.5 (P1/P0), (2)
603 the $\log_2$FC ≥ 1 (P3/P0), and (3) the difference of $\log_2$FC ≥ 0.5 (P3/P0−P1/P0). Such
604 cutoffs were applied to root PSI genes because the agriGO enrichment analysis (Tian *et*
605 *al.*, 2017) yielded a satisfactory list for further investigation, including nearly all *At*PHT1s
606 and more than ten other genes encoding transporters (Supporting Information Table S4).
607 Among the list, the PM-localized *At*OCT1, potassium transporter *At*HAK5
608 (AT4G13420), sulfate transporter *At*SULTR1;3 (AT1G22150), and the TP-localized Pi
609 transporter *At*VPE1 (AT3G47420) were selected for testing interaction with *At*CNIH5
610 based on the tripartite split-GFP association in agro-infiltrated *N. benthamiana* leaves
611 (Liu *et al.*, 2018; Liu, 2021). We also included *At*SOS, *At*URGT6, *At*DTX21, and
612 *At*DTX35 for testing but not *At*LRK10L-1.1 or *At*GXM2 due to the same membrane
613 topology of *At*CNIH5 and *At*GXM2 and the failure to find any agrobacteria transformants
614 carrying the *At*LRK10L-1.1 construct. The S10-tagged *At*CNIH5 (S10-*At*CNIH5) and the
615 S11-tagged fusion protein of interest correctly reached their subcellular destinations,
616 except that *At*SOS-S11 and *At*SULTR1;3-S11 were retained in the ER (Fig. **6a**).
617 Compared to the positive control *At*PHT1;1-S11 and the negative control 3xHA-S11 as
618 recently reported (Chiu *et al.*, 2024), S10-*At*CNIH5 interacted with *At*OCT1-S11, *At*SOS-
619 S11, *At*URGT6-S11, *At*DTX21-S11, and *At*DTX35-S11 *in planta*, yielding fluorescence
620 signals as a result of GFP complementation, but failed to interact with *At*HAK5-S11,
621 *At*SULTR1;3-S11, and *At*VPE1-S11 (Fig. **6b**). Taken together, our quantitative
622 proteomics successfully identified specific membrane cargoes of *At*CNIH5, including
623 *At*PHT1s.
624
625 **The C-terminal acidic residue of *At*CNIH5 is not required to interact with *At*PHT1;1**
626 As several *At*PHT1 members were identified as prominent cargoes of *At*CNIH5, we
627 were curious to find out which motif of *At*CNIH5 interacts with *At*PHT1;1. *At*CNIHs
628 have three putative TMD, with the N terminus facing the cytosol, the C terminus facing
629 the ER lumen, and at least four putative functional motifs (Wudick *et al.*, 2018; Chiu *et*
630 *al.*, 2024). The putative FLN motif in the second TMD of the yeast Erv14, known as a
631 cargo-binding site (Pagant *et al.*, 2015), is present in *At*CNIH2–4, denoted as the YLC
632 motif. The putative cytosolic IFRTL motif, located between the second and third TMD

633 of Erv14 and interacting with Sec24 (Powers & Barlowe, 2002), is also conserved in
634 *At*CNIH2–4 with several residues changed, denoted as the IFNNL motif. The C-terminal
635 acidic motif, which is only found in plants and fungi, is required for Erv14 to assist the
636 PM targeting of the yeast Nha1, Pdr12, and Qdr2 as well as for the rice *Os*CNIH1 to aid
637 the Golgi targeting of *Os*HKT1;3 (Rosas-Santiago *et al.*, 2017). Besides the cornichon
638 motif that is well conserved among all *At*CNIHs, *At*CNIH5 has the putative YLC and
639 IFNNL motifs with several residues changed and a shorter C-terminal putative acidic
640 motif with one aspartic acid residue (Supporting Information Fig. S5). We designed a
641 series of C-terminally truncated forms of *At*CNIH5. For unknown reasons, we failed to
642 obtain the clone expressing *At*CNIH5 1–102. Therefore, we only tested the interaction of
643 *At*PHT1;1 with *At*CNIH5 1–26, *At*CNIH5 1–49, *At*CNIH5 1–92, and *At*CNIH5 1–132 in
644 the yeast SUS (Fig. **7a**). *At*CNIH5 1–26, which contains only the first TMD, is sufficient
645 to interact with *At*PHT1;1. In comparison, *At*CNIH5 1–132, which has the last three
646 amino acids deleted (including the C-terminal aspartic acid), could still interact with
647 *At*PHT1;1 (Fig. **7b**). These results indicated that the putative C-terminal motif of
648 *At*CNIH5 is not necessary for interaction with *At*PHT1;1 and *At*CNIH5 employs a
649 different mechanism to interact with *At*PHT1;1 from those used by the fungi and rice
650 CNIHs for their cognate cargoes.
651
652 **Increasing *in-situ At*CNIH5 expression/activity enables robust plant growth**
653 Since the loss of *At*CNIH5 led to decreased abundance of *At*PHT1s (Table **2**),
654 inspecting whether overexpression of *At*CNIH5 can improve plant fitness under Pi
655 limitation was imperative. We found that the ectopic expression of RFP-*At*CNIH5, driven
656 by the cauliflower mosaic virus (CaMV) 35S promoter, resulted in distorted root
657 morphology (Supporting Information Fig. S6). This aberrant structure was likely caused
658 by deformation of the ER, a phenomenon previously associated with the overexpression
659 of Erv14 in budding yeast (Lagunas-Gomez *et al.*, 2023). Instead, the transgenic lines
660 expressing the genomic GFP-*AtCNIH5* fragment (*AtCNIH5pro*: GFP-*AtCNIH5*) in the
661 *cnih5* background restored the expression of *At*PHT1;1/2/3 to the WT-like level and grew
662 bigger than WT and *cnih5* when Pi is replete (Chiu *et al.*, 2024). We then systematically
663 examined the growth of these *cnih5* complemented lines under different Pi regimes.
664 Under Pi sufficiency and modest Pi deficiency—three days of Pi deprivation (0 μM Pi)

665 or eleven days of suboptimal Pi supply (50 μM Pi), the complemented *cnih5* lines
666 exhibited higher shoot and/or root fresh weight than the WT and *cnih5* plants (Fig. **8**). In
667 contrast, under severe Pi deficiency—eleven days of Pi deprivation (0 μM Pi), none of
668 the complemented lines had a larger shoot size than WT (Fig. **8**). Although we could
669 detect the expression of GFP-*AtCNIH5* proteins in the Pi-limited root of *cnih5*
670 complemented lines, it is technically difficult to discern whether GFP-*AtCNIH5* proteins
671 were more abundant than the endogenous *At*CNIH5 in WT (Supporting Information Fig.
672 S7). Nonetheless, the higher biomass of *cnih5* complemented lines likely results from
673 more efficient assimilation of acquired Pi due to increased GFP-*AtCNIH5*
674 expression/activity, along with the coordinated upregulation of *At*CNIH5 membrane
675 cargoes beyond *At*PHT1s. We thus inferred that a subtle increase of *in-situ* rather than
676 ectopic expression/activity of GFP-*AtCNIH5* suffices to activate downstream effectors of
677 *At*CNIH5, thereby boosting plant growth.
678

679 ## Discussion

680 CNIHs are the eukaryotic conserved cargo receptors that cycle between the ER and
681 the early Golgi to select membrane proteins for incorporation into COPII vesicles. In this
682 study, we aimed to discover potential membrane cargoes of low Pi-induced *At*CNIH5 by
683 iTRAQ-based proteomic analysis and, in the meantime, to provide the first membrane
684 proteome for *Arabidopsis* roots subjected to Pi deprivation (Zhou *et al.*, 2022). Given that
685 our iTRAQ-based proteomic analysis did not include Pi-sufficient WT and *cnih5*
686 samples, we sought to evaluate whether the identified potential membrane cargoes of
687 *At*CNIH5 are indeed PSI proteins. To address this, we examined the overlap between the
688 proteins we identified in the Pi-limited roots and the root PSI genes (P3/P0, FC > 1.5; Liu
689 et al., 2016). We found minimal overlap, at only 5.8%, between the 4317 identified
690 proteins and the root PSI genes (Supporting Information Table. S2), which aligned with
691 the previous study indicating a weak correlation between the protein and transcript
692 changes following Pi deficiency in *Arabidopsis* root (Lan *et al.*, 2012). Still, of the
693 integral MPs in the Pi-limited roots of *cnih5*, 7.8% (4 out of 51) of the upregulated and
694 32.3% (10 out of 31) of the downregulated proteins were classified as root PSI genes
695 (Supporting Information Table. S5). These results suggested that PSI genes are enriched
696 5.7-fold among the downregulated integral MPs in the Pi-limited roots of *cnih5* when

697 compared to the 4317 identified proteins. Therefore, the *At*CNIH5-dependent membrane
698 cargoes we identified are mainly associated with Pi starvation.
699 Considering that only integral MPs at the post-ER compartments are potential cargoes
700 of *At*CNIH5, we tested their interaction with *At*CNIH5. When expressed in the yeast
701 heterologous expression system, *At*CNIH5 interacted not only with the two major Pi
702 transporters for Pi uptake, *At*PHT1;1 and *At*PHT1;4 (Chiu *et al.*, 2024), but also with
703 *At*PHT1;2, *At*PHT1;5, *At*PHT1;7, and *At*PHT1;9 (Fig. **5a**), supporting that *At*PHT1s are
704 the prominent membrane cargoes of *At*CNIH5 under Pi starvation. This was not
705 surprising because the amino acid sequences of *At*PHT1s share over 47.4% identity. It
706 has been shown that the yeast and rice CNIHs used the C-terminal acidic motif to interact
707 with their cognate cargoes (Rosas-Santiago *et al.*, 2017). However, a recent study
708 revealed that the cargo binding motif of the pumpkin *Cm*CNIH1 may reside in the N-
709 terminal rather than the C-terminal region (Wei *et al.*, 2023). This agreed with our results
710 for *At*CNIH5 (Fig. **7b**), indicating that the TMD1 of *At*CNIH5 contains a motif that
711 interacts with *At*PHT1s.
712 Besides *At*PHT1s, we identified other PM-localized membrane proteins
713 downregulated in the Pi-limited roots of *cnih5*. *At*LRK10L-1.2 is involved in ABA
714 signaling (Lim *et al.*, 2015). The animal Son of Sevenless (SOS) proteins encode the
715 guanine nucleotide exchange factors acting on the Ras subfamily of small GTPases
716 (Bowtell *et al.*, 1992). However, the physiological role of SOS in plants remains to be
717 studied. The PSI *At*OCT1 was also identified as a cargo of *At*CNIH5. Intriguingly, the
718 *oct1* mutant exhibited enhanced root branching (Lelandais-Brière *et al.*, 2007),
719 phenocopying the higher lateral root density of *cnih5* (Chiu *et al.*, 2024). Although the
720 heterologous expression of *At*OCT1 in yeast could transport carnitine, it remains to be
721 determined which substrate *At*OCT1 transports that could negatively affect lateral root
722 development. Besides *At*URGT6 and *At*GXM2, various Golgi-localized TM proteins
723 involved in plant cell wall modification such as *At*QUL2 (AT2G03480) (Mouille *et al.*,
724 2007), *At*GAE1 (AT4G30440) (Mølhøj *et al.*, 2004), *At*GAUT3 (AT4G38270) (Sterling
725 *et al.*, 2006), and *At*TMN9 (AT5G25100) (Hiroguchi *et al.*, 2021), are remarkably
726 downregulated in the Pi-limited *cnih5* roots (Table **2**). By contrast, the Golgi-localized
727 hydroxyproline-O-galactosyltransferases *At*GALT9 (AT1G53290), which is involved in
728 pectin metabolism (Zhang *et al.*, 2021), is most highly and significantly upregulated in

729 the Pi-limited *cnih5* roots (Fig. **3d**). Previous analyses of root-specific co-expression have
730 indicated that early PSR genes are involved in cell wall remodeling, highlighting the
731 importance of this process in response to Pi deficiency (Liao *et al.*, 2011; Lin *et al.*,
732 2011). It is likely that *At*CNIH5 plays a critical role in Pi starvation-triggered cell wall
733 composition changes. Nevertheless, the difference in cell wall structure between WT and
734 *cnih5* awaits investigation. The TP-localized *At*DTX21 and *At*DTX35 were identified as
735 the potential cargoes of *At*CNIH5 (Fig. **5b** and **6b**). While *AtDTX35* is a PSI gene,
736 *AtDTX21* is co-induced with the type III effectors secreted by *Pseudomonas syringae* and
737 may mediate the detoxification of chlorinated herbicide atrazine (de Torres-Zabala *et al.*,
738 2007; Ramel *et al.*, 2007). More studies are required to unravel the physiological role of
739 *At*DTX21 and *At*DTX35 in Pi starvation responses. Intriguingly, *At*CNIH5 failed to
740 interact with many other manifest PSI transporters such as *At*HAK5, *At*SULTR1;3, and
741 *At*VPE1 (Fig. **5b**). In fact, we identified the PSI transporters *At*VPE1 and its paralog
742 *At*VPE3 in our proteomic analysis, but their expression did not differ between WT and
743 *cnih5* (Supporting Information Table S2), suggesting that *At*CNIH5 recognizes specific
744 PSI transporters through an unidentified mechanism.
745 In conclusion, an Azo-solubilized MME approach in conjunction with quantitative
746 proteomics was used to demonstrate the downregulation of *At*PHT1s and other membrane
747 proteins associated with Pi starvation in the roots of *cnih5* (Fig. **9**). Our analyses validated
748 the interaction between *At*CNIH5 and several membrane cargoes at post-ER
749 compartments, including *At*PHT1s, *At*OCT1, *At*URGT6, *At*DTX21, and *At*DTX35
750 transporters. We also showed that *At*CNIH5 increased in the Pi-depleted root as well as
751 in the Pi-replete root of *pho2*, likely due to a higher demand for the ER export of *At*PHT1s.
752 Moreover, introducing the genomic GFP-*AtCNIH5* fragment boosted plant growth across
753 a wide range of Pi supplies. Therefore, we propose that *At*CNIH5 acts as a Pi deficiency-
754 inducible hub to facilitate the ER-to-Golgi trafficking of specific membrane cargoes,
755 thereby improving plant fitness under suboptimal Pi availability.
756
757 **Accession Numbers**
758 Sequence data from this article can be found in the Arabidopsis Genome Initiative under
759 the following accession numbers: *At*CNIH5 (AT4G12090), *At*PHT1;1 (AT5G43350),
760 *At*PHT1;2 (AT5G43370), *At*PHT1;5 (AT2G32830), *At*PHT1;7 (AT3G54700), *At*PHT1;9

(AT1G76430), *At*LRK10L-1.1 (AT1G18390), *At*GXM2 (AT4G09990), *At*SOS (AT1G26650), *At*DTX21 (AT1G33110), *At*DTX35 (AT4G25640), *At*URGT6 (AT1G34020), *At*OCT1 (AT1G73220), *At*HAK5 (AT4G13420), *At*VPE1 (AT3G47420), *At*SULTR1;3 (AT1G22150).

Acknowledgments

This work was supported by the Ministry of Science and Technology (MOST 108-2311-B-007-003-MY3) and the National Science and Technology Council (NSTC 112-2313-B-007-001-MY3). We acknowledge Ms. He-Ting Yang for cloning the CDS of *At*OCT1, *At*HAK5, *At*VPE1, and *At*SULTR1;3, and Mr. Po-Ruey Huang for cloning the constructs expressing the truncated *At*CNIH5 variants. We also thank Mr. Cheng-Da Tsai for testing the interaction of PLVCub-*At*CNIH5 with NubG-*At*PHT1;2, NubG-*At*PHT1;5, NubG-*At*PHT1;7 and NubG-*At*PHT1;9. We thank Dr. Tzvy-Jen Chiou at Academia Sinica, Taiwan (R.O.C.), for sharing anti-PHO1 and anti-PHF1 antibodies and the technical support from the confocal imaging core (sponsored by MOST 110-2731-M-007-001), National Tsing Hua University.

Competing interests

None declared

Author contributions

T.-Y. L. conceived the project, designed the experiments, analyzed the experiments, and wrote the article. M.-H. T., J.-Y. W., H.-F. L., C.-Y. C., H.-X. C. and C.-A. L. performed and analyzed the experiments. T.-Y. L., M.-H. T. and J.-Y. W. contributed equally.

Data availability

All data supporting the findings of this study are available within the article and the Supporting Information (Figs S1–S7, Tabs S1–S5).

References

Abas L, Luschnig C (2010) Maximum yields of microsomal-type membranes from small amounts of plant material without requiring ultracentrifugation. Analytical Biochemistry **401:** 217-227

Arpat AB, Magliano P, Wege S, Rouached H, Stefanovic A, Poirier Y (2012)

Functional expression of PHO1 to the Golgi and *trans*-Golgi network and its role in export of inorganic phosphate. The Plant Journal **71:** 479-491

Barlowe CK, Miller EA (2013) Secretory Protein Biogenesis and Traffic in the Early Secretory Pathway. Genetics **193:** 383-410

Bayle V, Arrighi J-F, Creff A, Nespoulous C, Vialaret J, Rossignol M, Gonzalez E, Paz-Ares J, Nussaume L (2011) *Arabidopsis thaliana* High-Affinity Phosphate Transporters Exhibit Multiple Levels of Posttranslational Regulation. The Plant Cell **23:** 1523-1535

Bökel C, Dass S, Wilsch-Bräuninger M, Roth S (2006) *Drosophila* Cornichon acts as cargo receptor for ER export of the TGFα-like growth factor Gurken. Development **133:** 459-470

Bowtell D, Fu P, Simon M, Senior P (1992) Identification of murine homologues of the Drosophila son of sevenless gene: potential activators of ras. Proceedings of the National Academy of Sciences **89:** 6511-6515

Brown KA, Chen B, Guardado-Alvarez TM, Lin Z, Hwang L, Ayaz-Guner S, Jin S, Ge Y (2019) A photocleavable surfactant for top-down proteomics. Nature Methods **16:** 417-420

Brown KA, Tucholski T, Eken C, Knott S, Zhu Y, Jin S, Ge Y (2020) High-Throughput Proteomics Enabled by a Photocleavable Surfactant. Angewandte Chemie International Edition **59:** 8406-8410

Chen J, Wang Y, Wang F, Yang J, Gao M, Li C, Liu Y, Liu Y, Yamaji N, Ma JF, Paz-Ares J, Nussaume L, Zhang S, Yi K, Wu Z, Wu P (2015) The Rice CK2 Kinase Regulates Trafficking of Phosphate Transporters in Response to Phosphate Levels. The Plant Cell **27:** 711-723

Chiu C-Y, Tsai C-D, Wang J-Y, Tsai M-H, Kanno S, Lung H-F, Liu T-Y (2024) Phosphate Starvation-Induced CORNICHON HOMOLOG 5 as Endoplasmic Reticulum Cargo Receptor for PHT1 Transporters in *Arabidopsis*. bioRxiv**:** 2024.2006.2020.599911

Chopin F, Wirth J, Dorbe M-F, Lejay L, Krapp A, Gojon A, Daniel-Vedele F (2007) The Arabidopsis nitrate transporter AtNRT2.1 is targeted to the root plasma membrane. Plant Physiology and Biochemistry **45:** 630-635

Dancourt J, Barlowe C (2010) Protein Sorting Receptors in the Early Secretory Pathway. Annual Review of Biochemistry **79:** 777-802

de Torres-Zabala M, Truman W, Bennett MH, Lafforgue G, Mansfield JW, Rodriguez Egea P, Bögre L, Grant M (2007) *Pseudomonas syringae* pv. *tomato* hijacks the *Arabidopsis* abscisic acid signalling pathway to cause disease. The EMBO Journal **26:** 1434-1443

Evenson KJ, Post-Beittenmiller D (1995) Fatty Acid-Elongating Activity in Rapidly Expanding Leek Epidermis. Plant Physiology **109:** 707-716

Ge SX, Jung D, Yao R (2019) ShinyGO: a graphical gene-set enrichment tool for animals and plants. Bioinformatics **36:** 2628-2629

González E, Solano R, Rubio V, Leyva A, Paz-Ares J (2005) PHOSPHATE TRANSPORTER TRAFFIC FACILITATOR1 Is a Plant-Specific SEC12-Related Protein That Enables the Endoplasmic Reticulum Exit of a High-Affinity Phosphate Transporter in *Arabidopsis*. The Plant Cell **17:** 3500-3512

Hallgren J, Tsirigos KD, Pedersen MD, Almagro Armenteros JJ, Marcatili P, Nielsen H, Krogh A, Winther O (2022) DeepTMHMM predicts alpha and beta transmembrane proteins using deep neural networks. bioRxiv**:**

842 2022.2004.2008.487609
843 **Harmel N, Cokic B, Zolles G, Berkefeld H, Mauric V, Fakler B, Stein V, Klöcker N**
844 (2012) AMPA Receptors Commandeer an Ancient Cargo Exporter for Use as an
845 Auxiliary Subunit for Signaling. PLOS ONE **7:** e30681
846 **Hiroguchi A, Sakamoto S, Mitsuda N, Miwa K** (2021) Golgi-localized membrane
847 protein AtTMN1/EMP12 functions in the deposition of rhamnogalacturonan II
848 and I for cell growth in Arabidopsis. Journal of Experimental Botany **72:** 3611-
849 3629
850 **Hooper CM, Castleden IR, Tanz SK, Aryamanesh N, Millar AH** (2016) SUBA4: the
851 interactive data analysis centre for Arabidopsis subcellular protein locations.
852 Nucleic Acids Research **45:** D1064-D1074
853 **Huang T-K, Han C-L, Lin S-I, Chen Y-J, Tsai Y-C, Chen Y-R, Chen J-W, Lin W-**
854 **Y, Chen P-M, Liu T-Y, Chen Y-S, Sun C-M, Chiou T-J** (2013) Identification
855 of Downstream Components of Ubiquitin-Conjugating Enzyme PHOSPHATE2
856 by Quantitative Membrane Proteomics in *Arabidopsis* Roots. The Plant Cell **25:**
857 4044-4060
858 **Krogh A, Larsson B, von Heijne G, Sonnhammer ELL** (2001) Predicting
859 transmembrane protein topology with a hidden markov model: application to
860 complete genomes. Journal of Molecular Biology **305:** 567-580
861 **Kurokawa K, Nakano A** (2018) The ER exit sites are specialized ER zones for the
862 transport of cargo proteins from the ER to the Golgi apparatus. The Journal of
863 Biochemistry **165:** 109-114
864 **Lagunas-Gomez D, Yañez-Dominguez C, Zavala-Padilla G, Barlowe C, Pantoja O**
865 (2023) The C-terminus of the cargo receptor Erv14 affects COPII vesicle
866 formation and cargo delivery. Journal of Cell Science **136**
867 **Lan P, Li W, Schmidt W** (2012) Complementary Proteome and Transcriptome Profiling
868 in Phosphate-deficient Arabidopsis Roots Reveals Multiple Levels of Gene
869 Regulation. Molecular & Cellular Proteomics **11:** 1156-1166
870 **Lee C, Teng Q, Zhong R, Yuan Y, Haghighat M, Ye Z-H** (2012) Three Arabidopsis
871 DUF579 Domain-Containing GXM Proteins are Methyltransferases Catalyzing
872 4-*O*-Methylation of Glucuronic Acid on Xylan. Plant and Cell Physiology **53:**
873 1934-1949
874 **Lee S-B, Jung S-J, Go Y-S, Kim H-U, Kim J-K, Cho H-J, Park OK, Suh M-C** (2009)
875 Two Arabidopsis 3-ketoacyl CoA synthase genes, *KCS20* and *KCS2/DAISY*, are
876 functionally redundant in cuticular wax and root suberin biosynthesis, but
877 differentially controlled by osmotic stress. The Plant Journal **60:** 462-475
878 **Lelandais-Brière C, Jovanovic M, Torres GAM, Perrin Y, Lemoine R, Corre-**
879 **Menguy F, Hartmann C** (2007) Disruption of *AtOCT1*, an organic cation
880 transporter gene, affects root development and carnitine-related responses in
881 Arabidopsis. The Plant Journal **51:** 154-164
882 **Liao Y-Y, Buckhout TJ, Schmidt W** (2011) Phosphate deficiency-induced cell wall
883 remodeling. Plant Signaling & Behavior **6:** 700-702
884 **Lim CW, Yang SH, Shin KH, Lee SC, Kim SH** (2015) The AtLRK10L1.2, *Arabidopsis*
885 ortholog of wheat LRK10, is involved in ABA-mediated signaling and drought
886 resistance. Plant Cell Reports **34:** 447-455
887 **Lin W-D, Liao Y-Y, Yang TJW, Pan C-Y, Buckhout TJ, Schmidt W** (2011)
888 Coexpression-Based Clustering of Arabidopsis Root Genes Predicts Functional
889 Modules in Early Phosphate Deficiency Signaling. Plant Physiology **155:** 1383-

1402

Lin W-Y, Huang T-K, Chiou T-J (2013) NITROGEN LIMITATION ADAPTATION, a Target of MicroRNA827, Mediates Degradation of Plasma Membrane–Localized Phosphate Transporters to Maintain Phosphate Homeostasis in *Arabidopsis*. The Plant Cell **25:** 4061-4074

Liu T-Y (2021) Using Tripartite Split-sfGFP for the Study of Membrane Protein–Protein Interactions. *In* JJ Sanchez-Serrano, J Salinas, eds, Arabidopsis Protocols. Springer US, New York, NY, pp 323-336

Liu T-Y, Chou W-C, Chen W-Y, Chu C-Y, Dai C-Y, Wu P-Y (2018) Detection of membrane protein–protein interaction *in planta* based on dual-intein-coupled tripartite split-GFP association. The Plant Journal **94:** 426-438

Liu T-Y, Huang T-K, Tseng C-Y, Lai Y-S, Lin S-I, Lin W-Y, Chen J-W, Chiou T-J (2012) PHO2-Dependent Degradation of PHO1 Modulates Phosphate Homeostasis in *Arabidopsis*. The Plant Cell **24:** 2168-2183

Liu T-Y, Huang T-K, Yang S-Y, Hong Y-T, Huang S-M, Wang F-N, Chiang S-F, Tsai S-Y, Lu W-C, Chiou T-J (2016) Identification of plant vacuolar transporters mediating phosphate storage. Nature Communications **7:** 11095

Mølhøj M, Verma R, Reiter W-D (2004) The Biosynthesis of d-Galacturonate in Plants. Functional Cloning and Characterization of a Membrane-Anchored UDP-d-Glucuronate 4-Epimerase from Arabidopsis. Plant Physiology **135:** 1221-1230

Mouille G, Ralet M-C, Cavelier C, Eland C, Effroy D, Hématy K, McCartney L, Truong HN, Gaudon V, Thibault J-F, Marchant A, Höfte H (2007) Homogalacturonan synthesis in *Arabidopsis thaliana* requires a Golgi-localized protein with a putative methyltransferase domain. The Plant Journal **50:** 605-614

Nakanishi H, Suda Y, Neiman AM (2007) Erv14 family cargo receptors are necessary for ER exit during sporulation in *Saccharomyces cerevisiae*. Journal of Cell Science **120:** 908-916

Nguyen TV, Gupta R, Annas D, Yoon J, Kim Y-J, Lee GH, Jang JW, Park KH, Rakwal R, Jung K-H, Min CW, Kim ST (2021) An Integrated Approach for the Efficient Extraction and Solubilization of Rice Microsomal Membrane Proteins for High-Throughput Proteomics. Frontiers in Plant Science **12**

Nussaume L, Kanno S, Javot H, Marin E, Nakanishi TM, Thibaud M-C (2011) Phosphate Import in Plants: Focus on the PHT1 Transporters. Frontiers in Plant Science **2**

Obrdlik P, El-Bakkoury M, Hamacher T, Cappellaro C, Vilarino C, Fleischer C, Ellerbrok H, Kamuzinzi R, Ledent V, Blaudez D, Sanders D, Revuelta JL, Boles E, André B, Frommer WB (2004) K^+ channel interactions detected by a genetic system optimized for systematic studies of membrane protein interactions. Proceedings of the National Academy of Sciences **101:** 12242-12247

Pagant S, Wu A, Edwards S, Diehl F, Miller Elizabeth A (2015) Sec24 Is a Coincidence Detector that Simultaneously Binds Two Signals to Drive ER Export. Current Biology **25:** 403-412

Park BS, Seo JS, Chua N-H (2014) NITROGEN LIMITATION ADAPTATION Recruits PHOSPHATE2 to Target the Phosphate Transporter PT2 for Degradation during the Regulation of *Arabidopsis* Phosphate Homeostasis. The Plant Cell **26:** 454-464

Poirier Y, Bucher M (2002) Phosphate Transport and Homeostasis in Arabidopsis. The Arabidopsis Book **2002**

938 **Poirier Y, Jaskolowski A, Clúa J** (2022) Phosphate acquisition and metabolism in
939 plants. Current Biology **32:** R623-R629
940 **Powers J, Barlowe C** (1998) Transport of Axl2p Depends on Erv14p, an ER–Vesicle
941 Protein Related to the *Drosophila cornichon* Gene Product. Journal of Cell
942 Biology **142:** 1209-1222
943 **Powers J, Barlowe C** (2002) Erv14p Directs a Transmembrane Secretory Protein into
944 COPII-coated Transport Vesicles. Molecular Biology of the Cell **13:** 880-891
945 **R Core Team** (2021) R: A Language and Environment for Statistical Computing. R
946 Foundation for Statistical Computing
947 **Ramel F, Sulmon C, Cabello-Hurtado F, Taconnat L, Martin-Magniette M-L,**
948 **Renou J-P, El Amrani A, Couée I, Gouesbet G** (2007) Genome-wide
949 interacting effects of sucrose and herbicide-mediated stress in *Arabidopsis*
950 *thaliana*: novel insights into atrazine toxicity and sucrose-induced tolerance.
951 BMC Genomics **8:** 450
952 **Rosas-Santiago P, Lagunas-Gómez D, Barkla BJ, Vera-Estrella R, Lalonde S, Jones**
953 **A, Frommer WB, Zimmermannova O, Sychrová H, Pantoja O** (2015)
954 Identification of rice cornichon as a possible cargo receptor for the Golgi-
955 localized sodium transporter OsHKT1;3. Journal of Experimental Botany **66:**
956 2733-2748
957 **Rosas-Santiago P, Lagunas-Gomez D, Yáñez-Domínguez C, Vera-Estrella R,**
958 **Zimmermannová O, Sychrová H, Pantoja O** (2017) Plant and yeast cornichon
959 possess a conserved acidic motif required for correct targeting of plasma
960 membrane cargos. Biochimica et Biophysica Acta (BBA) - Molecular Cell
961 Research **1864:** 1809-1818
962 **Roth S, Shira Neuman-Silberberg F, Barcelo G, Schüpbach T** (1995) cornichon and
963 the EGF receptor signaling process are necessary for both anterior-posterior and
964 dorsal-ventral pattern formation in Drosophila. Cell **81:** 967-978
965 **RStudio Team** (2020) RStudio: Integrated Development Environment for R. RStudio,
966 PBC
967 **Saez-Aguayo S, Parra-Rojas JP, Sepúlveda-Orellana P, Celiz-Balboa J, Arenas-**
968 **Morales V, Sallé C, Salinas-Grenet H, Largo-Gosens A, North HM, Ralet M-**
969 **C, Orellana A** (2020) Transport of UDP-rhamnose by URGT2, URGT4, and
970 URGT6 modulates rhamnogalacturonan-I length. Plant Physiology **185:** 914-933
971 **Salazar-Henao JE, Schmidt W** (2016) An Inventory of Nutrient-Responsive Genes in
972 *Arabidopsis* Root Hairs. Frontiers in Plant Science **7**
973 **Sievers F, Wilm A, Dineen D, Gibson TJ, Karplus K, Li W, Lopez R, McWilliam H,**
974 **Remmert M, Söding J, Thompson JD, Higgins DG** (2011) Fast, scalable
975 generation of high-quality protein multiple sequence alignments using Clustal
976 Omega. Molecular Systems Biology **7:** 539
977 **Spitzer M, Wildenhain J, Rappsilber J, Tyers M** (2014) BoxPlotR: a web tool for
978 generation of box plots. Nature Methods **11:** 121-122
979 **Sterling JD, Atmodjo MA, Inwood SE, Kumar Kolli VS, Quigley HF, Hahn MG,**
980 **Mohnen D** (2006) Functional identification of an *Arabidopsis* pectin biosynthetic
981 homogalacturonan galacturonosyltransferase. Proceedings of the National
982 Academy of Sciences **103:** 5236-5241
983 **The UniProt Consortium** (2023) UniProt: the Universal Protein Knowledgebase in
984 2023. Nucleic Acids Research **51:** D523-D531
985 **Tian T, Liu Y, Yan H, You Q, Yi X, Du Z, Xu W, Su Z** (2017) agriGO v2.0: a GO

986 analysis toolkit for the agricultural community, 2017 update. Nucleic Acids
987 Research **45:** W122-W129
988 **Urbanowicz BR, Peña MJ, Ratnaparkhe S, Avci U, Backe J, Steet HF, Foston M, Li**
989 **H, O'Neill MA, Ragauskas AJ, Darvill AG, Wyman C, Gilbert HJ, York WS**
990 (2012) 4-*O*-methylation of glucuronic acid in *Arabidopsis* glucuronoxylan is
991 catalyzed by a domain of unknown function family 579 protein. Proceedings of
992 the National Academy of Sciences **109:** 14253-14258
993 **Wang X, Liang S** (2012) Sample preparation for the analysis of membrane proteomes
994 by mass spectrometry. Protein & Cell **3:** 661-668
995 **Waterhouse AM, Procter JB, Martin DMA, Clamp M, Barton GJ** (2009) Jalview
996 Version 2—a multiple sequence alignment editor and analysis workbench.
997 Bioinformatics **25:** 1189-1191
998 **Wei L, Liu L, Chen Z, Huang Y, Yang L, Wang P, Xue S, Bie Z** (2023) CmCNIH1
999 improves salt tolerance by influencing the trafficking of CmHKT1;1 in pumpkin.
1000 The Plant Journal **114:** 1353-1368
1001 **Wickham H, Chang W, Henry L, Lin Pedersen T, Takahashi K, Wilke C, Woo K,**
1002 **Yutani H, Dunnington D, van den Brand T** (2016) ggplot2: Elegant Graphics
1003 for Data Analysis. Springer-Verlag New York
1004 **Wu X, Lai Y, Rao S, Lv L, Ji M, Han K, Weng J, Lu Y, Peng J, Lin L, Wu G, Chen**
1005 **J, Yan F, Zheng H** (2021) Genome-Wide Identification Reveals That *Nicotiana*
1006 *benthamiana* Hypersensitive Response (HR)-Like Lesion Inducing Protein 4
1007 (NbHRLI4) Mediates Cell Death and Salicylic Acid-Dependent Defense
1008 Responses to Turnip Mosaic Virus. Frontiers in Plant Science **12**
1009 **Wudick MM, Portes MT, Michard E, Rosas-Santiago P, Lizzio MA, Nunes CO,**
1010 **Campos C, Santa Cruz Damineli D, Carvalho JC, Lima PT, Pantoja O, Feijó**
1011 **JA** (2018) CORNICHON sorting and regulation of GLR channels underlie pollen
1012 tube Ca^{2+} homeostasis. Science **360:** 533-536
1013 **Yáñez-Domínguez C, Lagunas-Gómez D, Torres-Cifuentes DM, Bezanilla M,**
1014 **Pantoja O** (2023) A cornichon protein controls polar localization of the PINA
1015 auxin transporter in *Physcomitrium patens*. Development **150**
1016 **Yang Z, Yang J, Wang Y, Wang F, Mao W, He Q, Xu J, Wu Z, Mao C** (2020)
1017 PROTEIN PHOSPHATASE95 Regulates Phosphate Homeostasis by Affecting
1018 Phosphate Transporter Trafficking in Rice. The Plant Cell **32:** 740-757
1019 **Yoshimoto K, Hanaoka H, Sato S, Kato T, Tabata S, Noda T, Ohsumi Y** (2004)
1020 Processing of ATG8s, Ubiquitin-Like Proteins, and Their Deconjugation by
1021 ATG4s Are Essential for Plant Autophagy. The Plant Cell **16:** 2967-2983
1022 **Yuan Y, Teng Q, Lee C, Zhong R, Ye Z-H** (2014) Modification of the degree of 4-*O*-
1023 methylation of secondary wall glucuronoxylan. Plant Science **219-220:** 42-50
1024 **Zhang H, Guo Z, Zhuang Y, Suo Y, Du J, Gao Z, Pan J, Li L, Wang T, Xiao L, Qin**
1025 **G, Jiao Y, Cai H, Li L** (2021) MicroRNA775 regulates intrinsic leaf size and
1026 reduces cell wall pectin levels by targeting a galactosyltransferase gene in
1027 Arabidopsis. The Plant Cell **33:** 581-602
1028 **Zhang H, Zhao F-G, Tang R-J, Yu Y, Song J, Wang Y, Li L, Luan S** (2017) Two
1029 tonoplast MATE proteins function as turgor-regulating chloride channels in
1030 *Arabidopsis*. Proceedings of the National Academy of Sciences **114:** E2036-
1031 E2045
1032 **Zheng J, Yao L, Zeng X, Wang B, Pan L** (2023) *ERV14* receptor impacts mycelial
1033 growth via its interactions with cell wall synthase and transporters in *Aspergillus*

1034 *niger*. Frontiers in Microbiology **14**
1035 **Zhou M, Zhu S, Mo X, Guo Q, Li Y, Tian J, Liang C** (2022) Proteomic Analysis
1036 Dissects Molecular Mechanisms Underlying Plant Responses to Phosphorus
1037 Deficiency. Cells **11:** 651
1038 **Zimmermannová O, Felcmanová K, Rosas-Santiago P, Papoušková K, Pantoja O,**
1039 **Sychrová H** (2019) Erv14 cargo receptor participates in regulation of plasma-
1040 membrane potential, intracellular pH and potassium homeostasis via its
1041 interaction with K^+-specific transporters Trk1 and Tok1. Biochimica et
1042 Biophysica Acta (BBA) - Molecular Cell Research **1866:** 1376-1388
1043

1044 **Supporting Information**

1045 **Fig. S1** Multiple marker abundance profiling (MMAP) of the identified proteins in Azo-
1046 solubilized microsomal protein extraction (MME) samples.
1047 (a) Summary of label-free proteomic analysis of microsomal proteins in *Arabidopsis* WT
1048 and *cnih5* Pi-limited roots.
1049 (b) Relative number of high confidence marker (hcm) proteins for each compartment.
1050 The relative number of distinct proteins for each compartment are displayed in the bar
1051 graph as a percentage of all unique proteins in Arabidopsis (Standard) or all proteins in
1052 the user sample (User).
1053 (c) Relative protein abundance of high hcm proteins for each compartment. The
1054 Normalized Gator Abundance Factor (NGAF) scores for each protein is summed per
1055 subcellular compartment according to the hcm assignments. The abundance-scaling
1056 factor for each compartment describes the skew between the standard observations in
1057 Arabidopsis (Standard) and the estimated abundance observation in the user sample. The
1058 NGAF scores for each protein in the user sample is multiplied by the compartmental
1059 scaling factor and summed per subcellular compartment according to the hcm list. The
1060 sums for each compartment are displayed in the bar graph as a percentage of the whole
1061 protein abundance (Standard) or all proteins in the total user sample (User).
1062

1063 **Fig. S2** Gene ontology (GO) analysis of the 4,317 identified proteins in iTRAQ-based
1064 proteomics of *Arabidopsis* WT and *cnih5* Pi-limited roots.
1065 Dot plots of the top GO terms in enrichment analysis for categories of molecular function
1066 (MF), biological process (BP), and cellular component (CC) ranked by fold enrichment.
1067 Fold enrichment compares the sample frequency representing the number of genes
1068 inputted under each GO term to the background frequency of total genes annotated to the

1069 same term in *A. thaliana*. The size of the dot indicates the number of genes in each GO
1070 term. The more intense reddish color reflects a lower adjusted *p*-value shown by
1071 $-\log_{10}$(FDR).
1072
1073 **Fig. S3** GO and KEGG pathway enrichment analyses of the 372 upregulated proteins and
1074 the 51 upregulated integral microsomal proteins (MPs) in the Pi-limited root of *cnih5*.
1075 (a, b) Dot plots of the gene ontology (GO) analyses of the 372 upregulated proteins (a)
1076 and the 51 upregulated integral MPs (b) ranked by fold enrichment for categories of
1077 molecular function, biological process, and cellular component.
1078 (c, d) Dot plots of the KEGG pathway analyses of the 372 upregulated proteins (c) and
1079 the 51 upregulated integral MPs (d) ranked by fold enrichment. Fold enrichment
1080 compares the sample frequency representing the number of genes inputted under each
1081 GO term or KEGG term to the background frequency of total genes annotated to the same
1082 term in *A. thaliana*. The size of the dot indicates the number of genes in each GO term or
1083 KEGG term. The more intense reddish color reflects a lower adjusted *p*-value shown by
1084 $-\log_{10}$ (FDR).
1085
1086 **Fig. S4** Analysis of the interaction of PLVCub-*At*CNIH5 with NubG-*At*SOS, NubG-
1087 *At*OCT1, NubG-*At*URGT6, NubG-*At*DTX21, and NubG-*At*DTX35 using the yeast split-
1088 ubiquitin system (SUS). The co-expression of PLVCub-*At*CNIH5 with NubI and NubG
1089 are used as positive and negative controls, respectively. Yeast transformants were grown
1090 on synthetic medium without leucine and tryptophan (–LW; the left panel) or on synthetic
1091 medium lacking leucine, tryptophan, and adenine with 500 μM methionine (–LWAH; the
1092 middle panel) or on SC–LW containing 100 mg/L X-Gal (X-Gal; the right panel).
1093
1094 **Fig. S5** Amino acid sequence alignment of *Sc*Erv14 and *At*CNIHs.
1095 The sequence alignment was performed using the Clustal Omega algorithm (Sievers *et*
1096 *al.*, 2011) and visualized using Jalview version 2.11.4.0 (Waterhouse *et al.*, 2009). The
1097 degree of amino acid conservation among the CNIHs is represented by a light-to-dark
1098 blue color gradient. The transmembrane domains (TMD) are boxed by solid lines. The
1099 putative cornichon, YLC, IFNLL, and acidic motifs are boxed by dotted lines. The protein
1100 sequences were retrieved from UniprotKB (Uniprot ID: *Sc*Erv14, P53173; *At*CNIH1,

1101 Q9C7D7; *At*CNIH2, Q3EDD7; *At*CNIH3, Q8GWT5; *At*CNIH4, Q84W04; *At*CNIH5,
1102 Q9SZ74).
1103
1104 **Fig. S6** Expression of *35S:* RFP-*At*CNIH5 in *Arabidopsis*.
1105 Expression of *35S*: RFP-*At*CNIH5 in 5-day-old *Arabidopsis* seedlings grown under Pi-
1106 deficient (–P, 0 μM KH_2PO_4, five days of starvation) conditions. Scale bars, 50 μm.
1107
1108 **Fig. S7** Protein expression of the endogenous *At*CNIH5 in WT and GFP-*AtCNIH5* in the
1109 *AtCNIH5pro*: GFP-*AtCNIH5/cnih5* complementation (COM) plants under Pi deficiency.
1110 Immunoblot analysis of *At*CNIH5 and GFP-*AtCNIH5* in the root of *Arabidopsis* 11-day-
1111 old WT and COM seedlings under Pi-deficient (–P, 0 μM KH_2PO_4, seven days of
1112 starvation) conditions. The bands of *At*CNIH5 and GFP-*AtCNIH5* are indicated by solid
1113 arrowhead and open arrowhead, respectively.
1114
1115 **Table S1.** Oligonucleotides used for plasmid constructs.
1116
1117 **Table S2.** A list of the identified 4317 proteins in *Arabidopsis* Pi-limited WT and *cnih5*
1118 roots with GO enrichment analysis.
1119 Detailed descriptions of our proteomic analysis, including the protein scores and mass,
1120 annotation, predicted transmembrane helices, quantification for the identified proteins,
1121 and a list of the 61 overlapped identified proteins between our datasets and the Pi
1122 starvation root proteome by (Lan *et al.*, 2012).
1123
1124 **Table S3.** A list of the 372 upregulated and 106 downregulated proteins in Pi-limited
1125 *cnih5* roots with GO enrichment analysis.
1126 Detailed descriptions, including annotation, predicted transmembrane helices, and
1127 quantification for the proteins identified in proteomic analysis.
1128
1129 **Table S4.** A list of the 19 root Pi starvation-induced (PSI) genes encoding transporters.
1130 **Table S5.** Enrichment of root Pi starvation-induced (PSI) genes in the iTRAQ-based
1131 proteomic analysis.
1132

1133 **Figure legends**

1134 **Figure 1.** iTRAQ-based quantitative proteomic analysis of Pi-limited *Arabidopsis* roots.
1135 (a) Schematic workflow of Azo-solubilized microsomal protein extraction for iTRAQ-
1136 based quantitative proteomic analysis of *Arabidopsis* Pi-limited roots.
1137 (b) UV-Vis spectrum monitoring the degradation of 1% Azo as a function of UV
1138 irradiation time.
1139

1140 **Figure 2.** Immunoblot analysis of root microsomal proteins extracted from WT, *cnih5*,
1141 and *pho2* mutants.
1142 (a, b) Protein expression of *At*PHF1, *At*PHO1, *At*PHT1;1/2/3, and *At*NRT2.1 (a) and
1143 *At*CNIH5 (b) in the root of 11-day-old seedlings of *Arabidopsis* WT, *cnih5*, and *pho2*
1144 under Pi-sufficient (+P) and Pi-deficient (–P, 0 μM KH_2PO_4, five days of starvation)
1145 conditions. The band of *At*CNIH5 is indicated by arrowhead. The relative protein
1146 expression level was normalized with the corresponding amido black staining and relative
1147 to the WT control. Error bars represent SE (n = 2–4). The applied extraction methods
1148 were shown as indicated.
1149

1150 **Figure 3.** Summary of iTRAQ-based proteomic analysis of microsomal proteins (MPs)
1151 in Pi-limited WT and *cnih5* roots.
1152 (a) Venn diagram for comparing MPs and transmembrane (TM) proteins of the 4317
1153 identified proteins. Subcellular localization was analyzed by SUBA5. TM protein
1154 prediction or annotation was performed by deepTMHMM or UniprotKB.
1155 (b) Distribution of subcellular localizations of the identified 4317 proteins analyzed by
1156 SUBA5. Note that not all proteins are restricted to a single subcellular location.
1157 (c) Distribution of subcellular localizations of the 915 integral MPs among the identified
1158 1231 TM proteins analyzed by SUBA5. Note that not all proteins are restricted to a single
1159 subcellular location.
1160 (d) Volcano plots of differentially expressed proteins (DEPs) in the Pi-limited root of
1161 *cnih5*. Results of the four comparison groups (four ratios of *cnih5* versus WT) were
1162 shown separately, with the $-\log_{10}$FDR adj. *p*-value plotted against the $\log_2$ fold-change
1163 (FC). The vertical dash lines denote ±1.25-FC (Log_2 FC ≈ 0.322 and Log_2FC ≈ −0.415),
1164 while the horizontal dash line denotes FDR adj. *p*-value = 0.05. Upregulated and

1165 downregulated proteins are, respectively, indicated by red and blue dots. Only DEPs with
1166 ±2-FC are marked in red or blue. The *At*PHT1s and *At*PHF1 are marked in green. The
1167 proteins used for interaction testing are marked in purple.
1168
1169 **Figure 4.** GO and KEGG pathway enrichment analyses of the 106 downregulated
1170 proteins in Pi-limited *cnih5* roots.
1171 (a) Dot plots of the GO enrichment analysis ranked by fold enrichment for categories of
1172 molecular function, biological process, and cellular component.
1173 (b) Dot plots of the KEGG pathway enrichment analysis ranked by fold enrichment. Fold
1174 enrichment compares the sample frequency representing the number of genes inputted
1175 under each GO term or KEGG term to the background frequency of total genes annotated
1176 to the same term in *A. thaliana*. The size of the dot indicates the number of genes in each
1177 GO term or KEGG term. The more intense reddish color reflects a lower adj. *p*-value
1178 adjusted *p*-value shown by $-\log_{10}$(FDR).
1179
1180 **Figure 5.** Analysis of the interaction of *At*CNIH5 with its potential ER cargoes by the
1181 yeast split-ubiquitin system.
1182 (a) Co-expression of PLVCub-*At*CNIH5 with NubG-*At*PHT1;2, NubG-*At*PHT1;5,
1183 NubG-*At*PHT1;7, and NubG-*At*PHT1;9.
1184 (b) Co-expression of PLVCub-*At*CNIH5 with *At*LRK10L-1.1-NubG, *At*SOS-NubG,
1185 *At*OCT1-NubG, *At*URGT6-NubG, NubG-*At*GXM2, *At*DTX21-NubG, and *At*DTX35-
1186 NubG. The co-expression of PLVCub-*At*CNIH5 with NubI and NubG are used as positive
1187 and negative controls, respectively. Yeast transformants were grown on synthetic
1188 medium without leucine and tryptophan (–LW; the left panel) or on synthetic medium
1189 lacking leucine, tryptophan, adenine, and histidine with 500 μM methionine (–LWAH;
1190 middle panel) or on SC–LW containing 100 mg/L X-Gal (X-Gal; the right panel).
1191
1192 **Figure 6.** Analysis of the interaction of *At*CNIH5 with its potential ER cargoes by the
1193 tripartite split-GFP assay in *N. benthamiana* leaves.
1194 (a, b) Subcellular localization (a) and protein–protein interaction analysis (b) of S10-
1195 *At*CNIH5, *At*PHT1;1-S11, 3xHA-S11, *At*SOS-S11, *At*OCT1-S11, *At*HAK5-S11,
1196 *At*SULTR1;3-S11, *At*URGT6-S11, *At*DTX21-S11, *At*DTX35-S11, and *At*VPE1-S11.

1197 The co-expression of S10-*At*CNIH5 with *At*PHT1;1-S11 and 3xHA-S11 are used as
1198 positive and negative controls, respectively. The percentage of laser power used for
1199 acquisition is shown. Scale bars, 5 μm.
1200
1201 **Figure 7**. Analysis of the interaction of *At*PHT1;1 and the truncated *At*CNIH5 variants
1202 by the yeast split ubiquitin assay.
1203 (a) Schematic diagram of full-length (FL) and truncated *At*CNIH5 variants. The lengths
1204 of the truncated variants are indicated by the number of residues. The transmembrane
1205 domains and the putative cornichon, YLC, IFNLL, and acidic motifs are shown. The
1206 black box, the transmembrane domain (TMD); the blue box, the cornichon motif; the
1207 green box, the YLC motif; the yellow box, the IFNLL motif. The red box, the acidic
1208 motif. The gray box shows the sequence alignment of the putative acidic motif of *Sc*Erv14
1209 and *At*CNIHs. Noted that *At*CNIH5 has a shorter C-terminal tail carrying only one acidic
1210 residue D134.
1211 (b) Co-expression of *At*PHT1;1-PLVCub with NubG-*At*CNIH5, NubG-*At*CNIH5 1–26,
1212 NubG-*At*CNIH5 1–49, NubG-*At*CNIH5 1–92, and NubG-*At*CNIH5 1–132. The co-
1213 expression of *At*PHT1;1-PLVCub with NubI and NubG are used as positive and negative
1214 controls, respectively. Yeast transformants were grown on synthetic medium without
1215 leucine and tryptophan (–LW; the left panel) or on synthetic medium lacking leucine,
1216 tryptophan, adenine, and histidine with 500 μM methionine (–LWAH; middle panel) or
1217 on SC–LW containing 100 mg/L X-Gal (X-Gal; the right panel).
1218
1219 **Figure 8**. Increasing *in-situ At*CNIH5 expression/activity boosts plant growth.
1220 The shoot and root fresh weight (FW) of *Arabidopsis* 11-day-old WT, *cnih5* and
1221 *AtCNIH5pro*: GFP-*AtCNIH5/cnih5* complementation (COM) lines under Pi-sufficient
1222 (+P, 250 μM KH_2PO_4), modest Pi-deficient (–P, 0 μM KH_2PO_4, three days of starvation
1223 or 50 μM KH_2PO_4, eleven days of starvation), and severe Pi-deficient (–P, 0 μM KH_2PO_4,
1224 eleven days of starvation) conditions. Data are visualized using BoxPlotR (Spitzer *et al.*,
1225 2014). Center lines show the medians; the central plus signs (+) show the means; box
1226 limits indicate the 25th and 75th percentiles; whiskers extend to the 5th and 95th
1227 percentiles, and data points are plotted as dots. Data significantly different from the other
1228 groups are indicated by different lowercase letters (n, pools of seedings from independent

1229 experiments; One-Way ANOVA, Duncan's test).

1230

1231 **Figure 9**. *At*CNIH5-mediated ER-to-Golgi transport of membrane proteins associated
1232 with Pi starvation responses in *Arabidopsis* root.
1233 Under Pi starvation (−P), the transcripts of *CNIH5*, *PHT1* genes, *OCT1*, *GXM2*, and
1234 *DTX35* increase in *Arabidopsis* root cells (Liu *et al.*, 2016). As an ER cargo receptor,
1235 CNIH5 assists the ER export of the newly synthesized PHT1s, LRK10L-1.1, SOS, OCT1,
1236 URGT6, GXM2, DTX21, and DTX35 and their loading into COPII vesicles, thus their
1237 corresponding subcellular destinations.

1238

1239 **Table 1.** Summary of *At*PHT1s and *At*PHF1 expression in Pi-limited WT and *cnih5* roots.
1240 The normalized ratios compared the protein expression in Col-0_1, Col-0_2, *cnih5*_1,
1241 and *cnih5*_2 samples. The FDR adj. *p*-values were in the parentheses.

1242

1243 **Table 2.** List of the 31 downregulated microsomal transmembrane proteins in Pi-limited
1244 *cnih5* roots.
1245 The normalized ratios compared the protein expression in Col-0_1, Col-0_2, *cnih5*_1,
1246 and *cnih5*_2 samples. The FDR adj. *p*-values were in the parentheses. The candidates
1247 highlighted in gray were selected for testing protein–protein interaction in this study.
1248 Subcellular localization is predicted or annotated by SUBA5, UniprotKB or experimental
1249 data.

1250

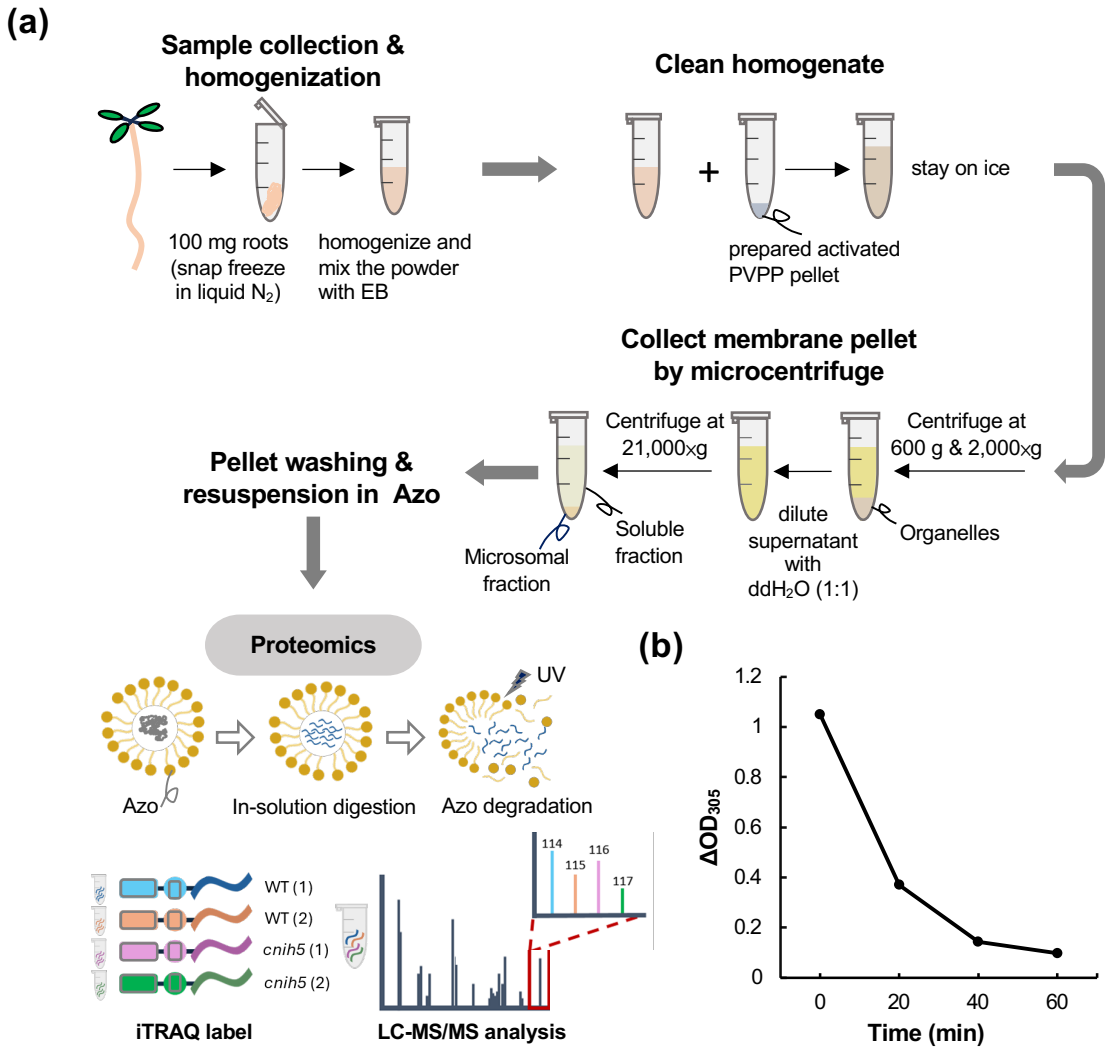

Figure 1. iTRAQ-based quantitative proteomic analysis of Pi-limited *Arabidopsis* roots.
(a) Schematic workflow of Azo-solubilized microsomal protein extraction for iTRAQ-based quantitative proteomic analysis of *Arabidopsis* Pi-limited roots.
(b) UV-Vis spectrum monitoring the degradation of 1% Azo as a function of UV irradiation time.

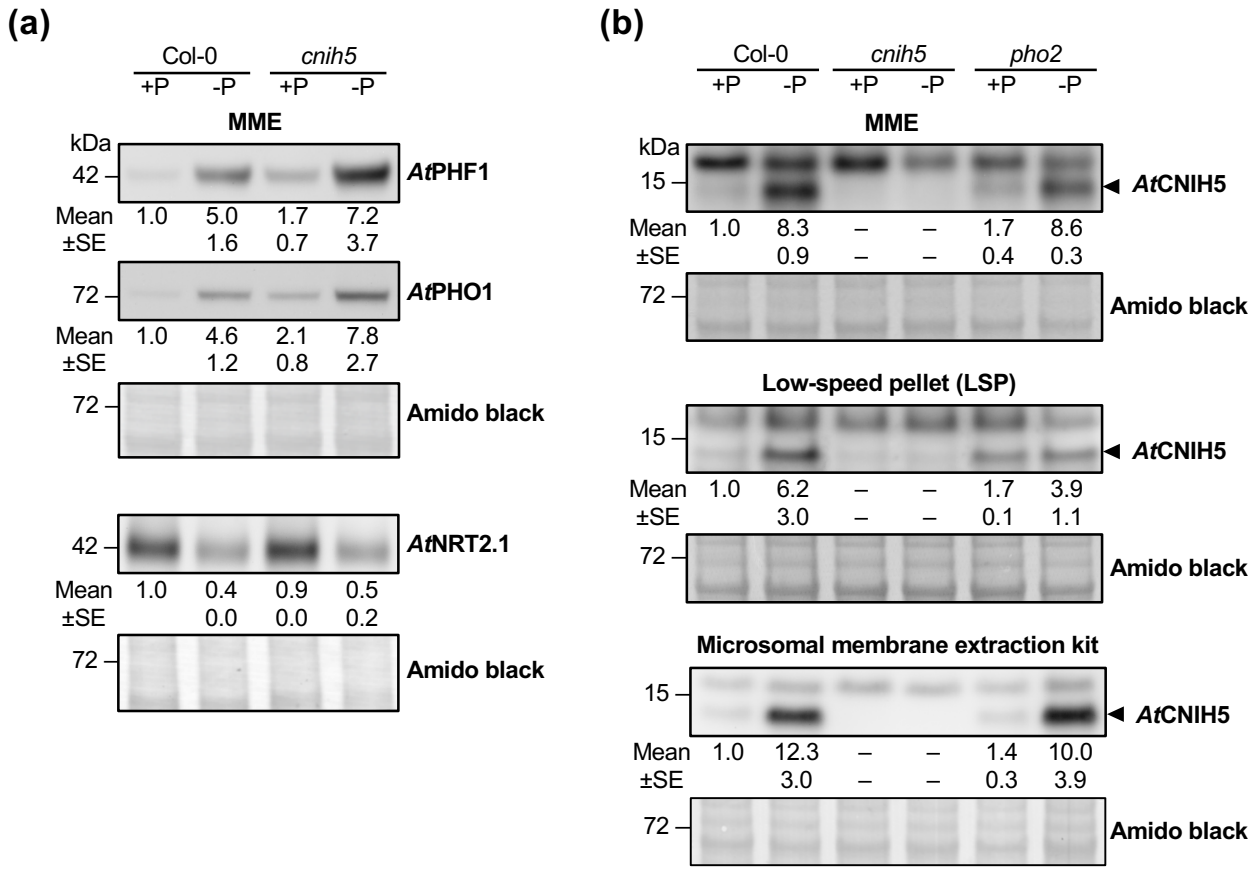

Figure 2. Immunoblot analysis of root microsomal proteins extracted from WT, *cnih5*, and *pho2* mutants.
(a and b) Protein expression of *At*PHF1, *At*PHO1, and *At*NRT2.1 (a) and *At*CNIH5 (b) in the root of 11-day-old seedlings of *Arabidopsis* WT, *cnih5*, and *pho2* under Pi-sufficient (+P) and Pi-deficient (–P, 0 μM KH_2PO_4, five days of starvation) conditions. The band of *At*CNIH5 is indicated by arrowhead. The relative protein expression level was normalized with the corresponding amido black staining and relative to the WT control. Error bars represent SE (n = 2–4). The applied extraction methods were shown as indicated.

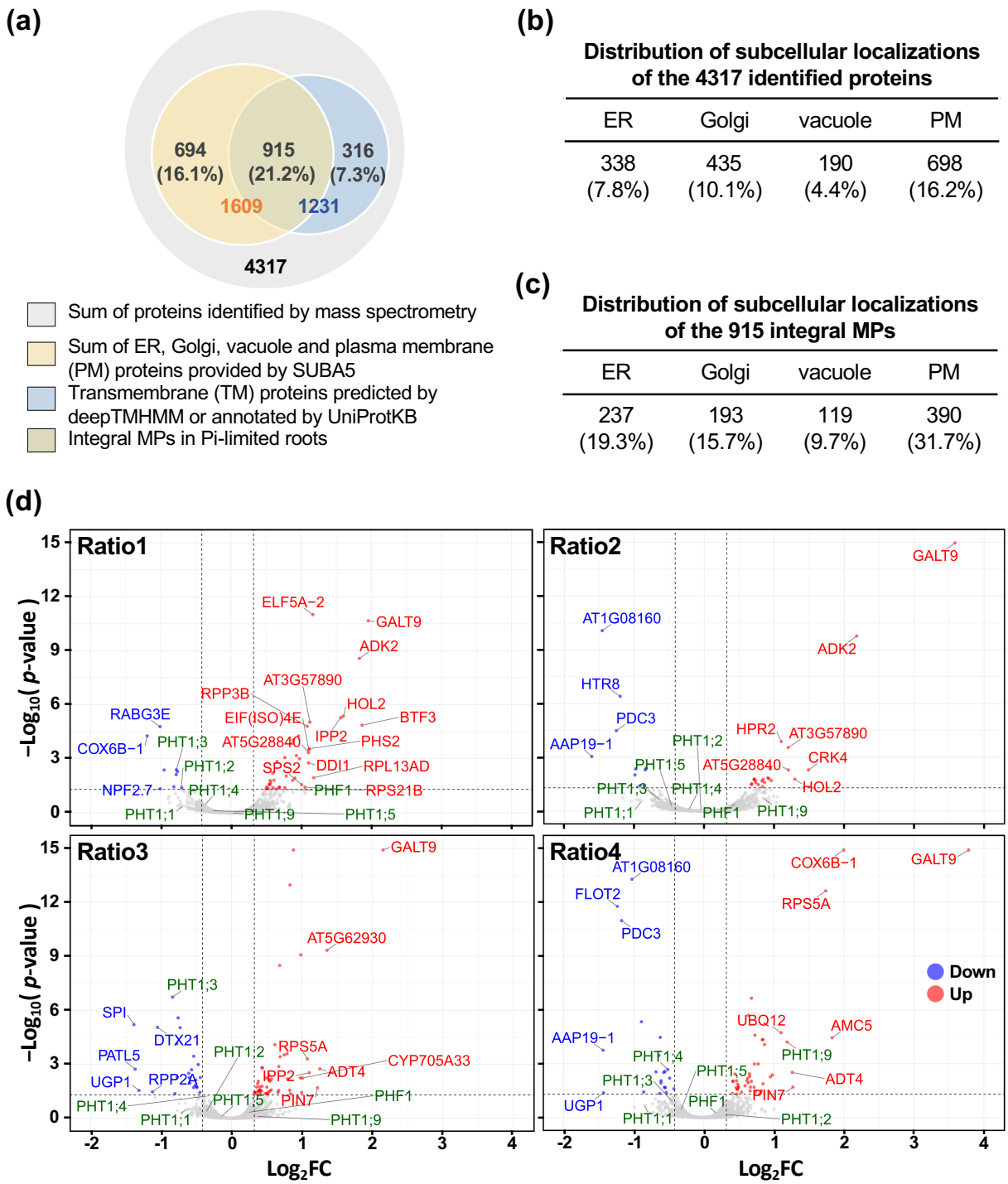

Figure 3. Summary of iTRAQ-based proteomic analysis of microsomal proteins (MPs) in Pi-limited WT and *cnih5* roots.

(a) Venn diagram for comparing MPs and transmembrane (TM) proteins of the 4317 identified proteins. Subcellular localization was analyzed by SUBA5. TM protein prediction or annotation was performed by deepTMHMM or UniprotKB.

(b) Distribution of subcellular localizations of the identified 4317 proteins analyzed by SUBA5. Note that not all proteins are restricted to a single subcellular location.

(c) Distribution of subcellular localizations of the 915 integral MPs among the identified 1231 TM proteins analyzed by SUBA5. Note that not all proteins are restricted to a single subcellular location.

(d) Volcano plots of differentially expressed proteins (DEPs) in the Pi-limited root of *cnih5*. Results of the four comparison groups (four ratios of *cnih5* versus WT) were shown separately, with the $-\log_{10}$FDR adj. *p*-value plotted against the $\log_2$ fold-change (FC). The vertical dash lines denote ±1.25-FC (Log_2 FC ≈ 0.322 and Log_2FC ≈ −0.415), while the horizontal dash line denotes FDR adj. *p*-value = 0.05. Upregulated and downregulated proteins are, respectively, indicated by red and blue dots. Only DEPs with ±2-FC are specified in red or blue. The *At*PHT1s and *At*PHF1 are marked in green. The proteins used for interaction testing are marked in purple.

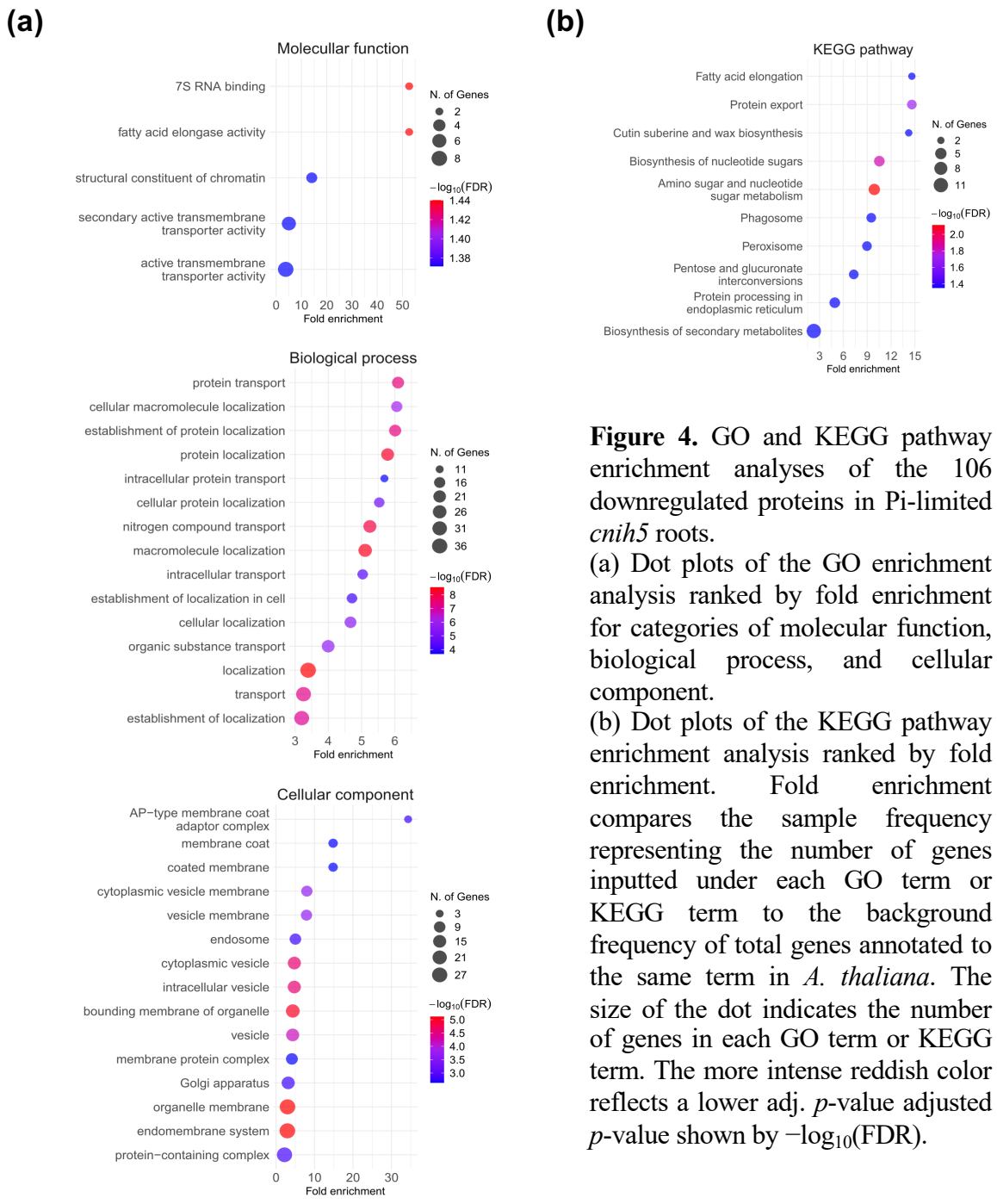

Figure 4. GO and KEGG pathway enrichment analyses of the 106 downregulated proteins in Pi-limited *cnih5* roots.
(a) Dot plots of the GO enrichment analysis ranked by fold enrichment for categories of molecular function, biological process, and cellular component.
(b) Dot plots of the KEGG pathway enrichment analysis ranked by fold enrichment. Fold enrichment compares the sample frequency representing the number of genes inputted under each GO term or KEGG term to the background frequency of total genes annotated to the same term in *A. thaliana*. The size of the dot indicates the number of genes in each GO term or KEGG term. The more intense reddish color reflects a lower adj. *p*-value adjusted *p*-value shown by $-\log_{10}$(FDR).

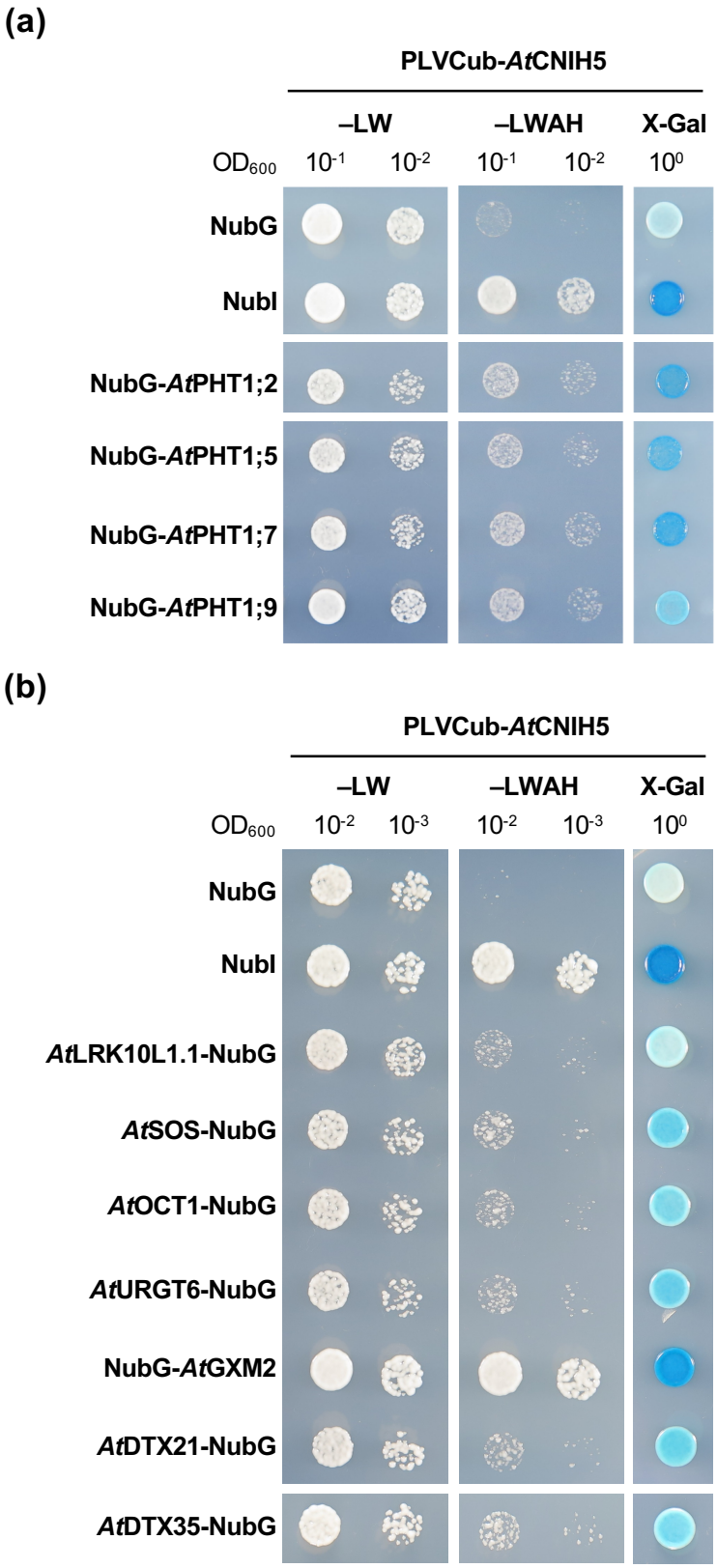

Figure 5. Analysis of the interaction of *At*CNIH5 with its potential ER cargoes by the yeast split-ubiquitin system.
(a) Co-expression of PLVCub-*At*CNIH5 with NubG-*At*PHT1;2, NubG-*At*PHT1;5, NubG-*At*PHT1;7, and NubG-*At*PHT1;9.
(b) Co-expression of PLVCub-*At*CNIH5 with *At*LRK10L-1.1-NubG, *At*SOS-NubG, *At*OCT1-NubG, *At*URGT6-NubG, NubG-*At*GXM2, *At*DTX21-NubG, and *At*DTX35- NubG. The co-expression of PLVCub-*At*CNIH5 with NubI and NubG are used as positive and negative controls, respectively. Yeast transformants were grown on synthetic medium without leucine and tryptophan (–LW; the left panel) or on synthetic medium lacking leucine, tryptophan, adenine, and histidine with 500 μM methionine (–LWAH; middle panel) or on SC–LW containing 100 mg/L X-Gal (X-Gal; the right panel).

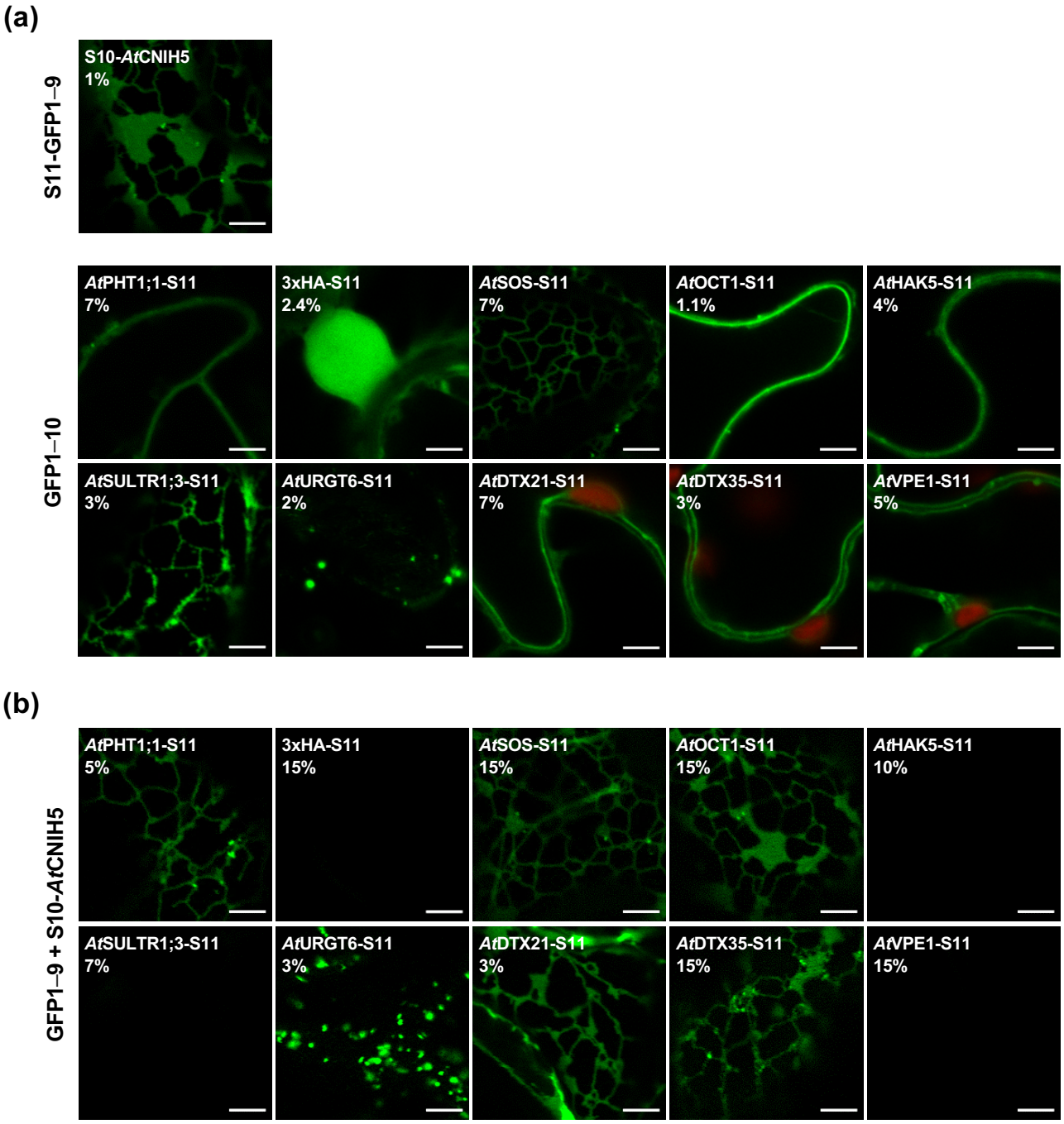

Figure 6. Analysis of the interaction of *At*CNIH5 with its potential ER cargoes by the tripartite split-GFP assay in *N. benthamiana* leaves.
(a and b) Subcellular localization (a) and protein–protein interaction analysis (b) of S10-*At*CNIH5, *At*PHT1;1-S11, 3xHA-S11, *At*SOS-S11, *At*OCT1-S11, *At*HAK5-S11, *At*SULTR1;3-S11, *At*URGT6-S11, *At*DTX21-S11, *At*DTX35-S11, and *At*VPE1-S11. The co-expression of S10-*At*CNIH5 with *At*PHT1;1-S11 and 3xHA-S11 are used as positive and negative controls, respectively. The percentage of laser power used for acquisition is shown. Scale bars, 5 μm.

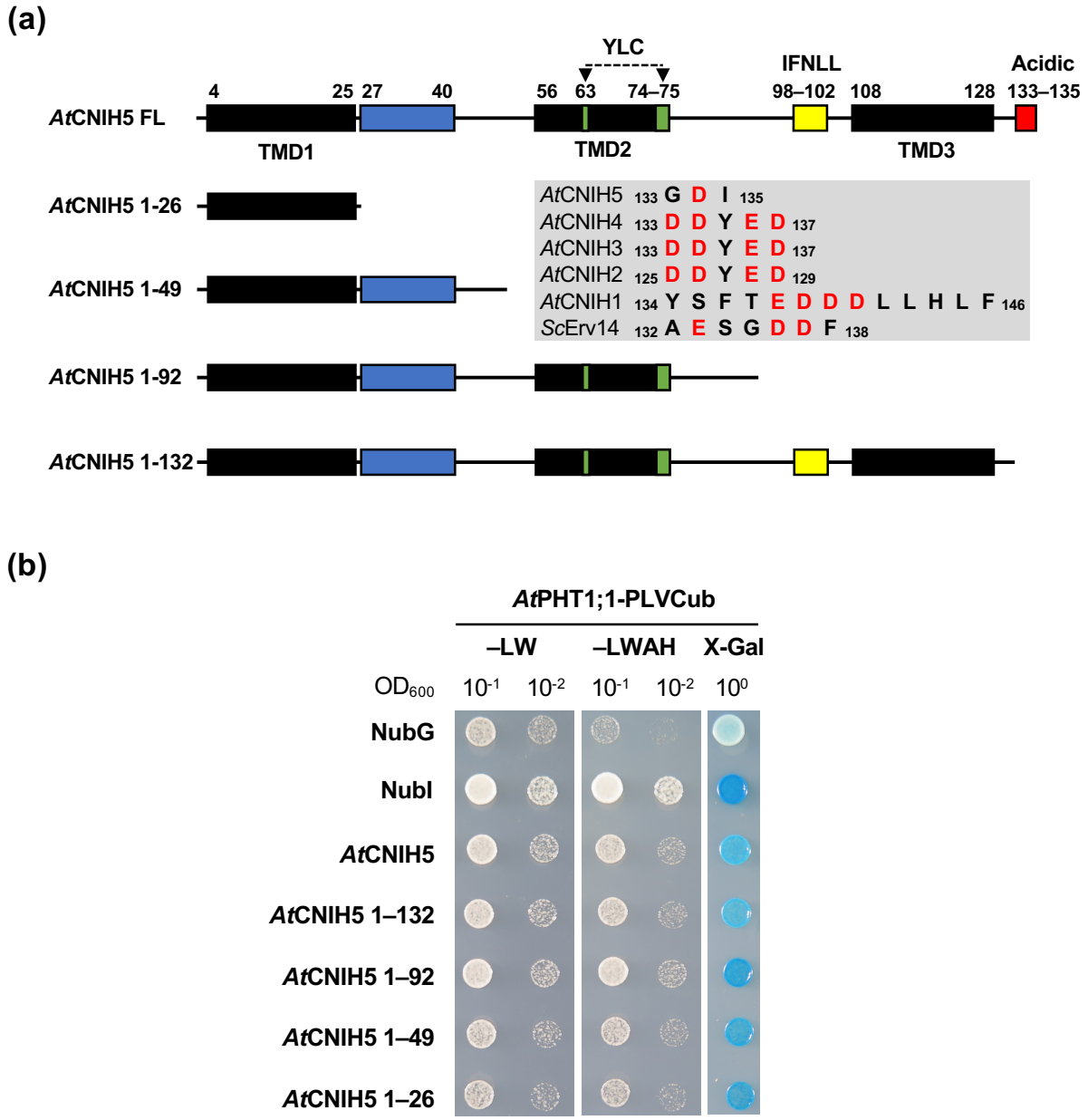

Figure 7. Analysis of the interaction of *At*PHT1;1 and the truncated *At*CNIH5 variants by the yeast split ubiquitin assay.

(a) Schematic diagram of full-length (FL) and truncated *At*CNIH5 variants. The lengths of the truncated variants are indicated by the number of residues. The transmembrane domains and the putative cornichon, YLC, IFNLL, and acidic motifs are shown. The black box, the transmembrane domain (TMD); the blue box, the cornichon motif; the green box, the YLC motif; the yellow box, the IFNLL motif. The red box, the acidic motif. The gray box shows the sequence alignment of the putative acidic motif of *Sc*Erv14 and *At*CNIHs. Noted that *At*CNIH5 has a shorter C-terminal tail carrying only one acidic residue D134.

(b) Co-expression of *At*PHT1;1-PLVCub with NubG-*At*CNIH5, NubG-*At*CNIH5 1–26, NubG-*At*CNIH5 1–49, NubG-*At*CNIH5 1–92, and NubG-*At*CNIH5 1–132. The co-expression of *At*PHT1;1-PLVCub with NubI and NubG are used as positive and negative controls, respectively. Yeast transformants were grown on synthetic medium without leucine and tryptophan (–LW; the left panel) or on synthetic medium lacking leucine, tryptophan, adenine, and histidine with 500 μM methionine (–LWAH; middle panel) or on SC–LW containing 100 mg/L X-Gal (X-Gal; the right panel).

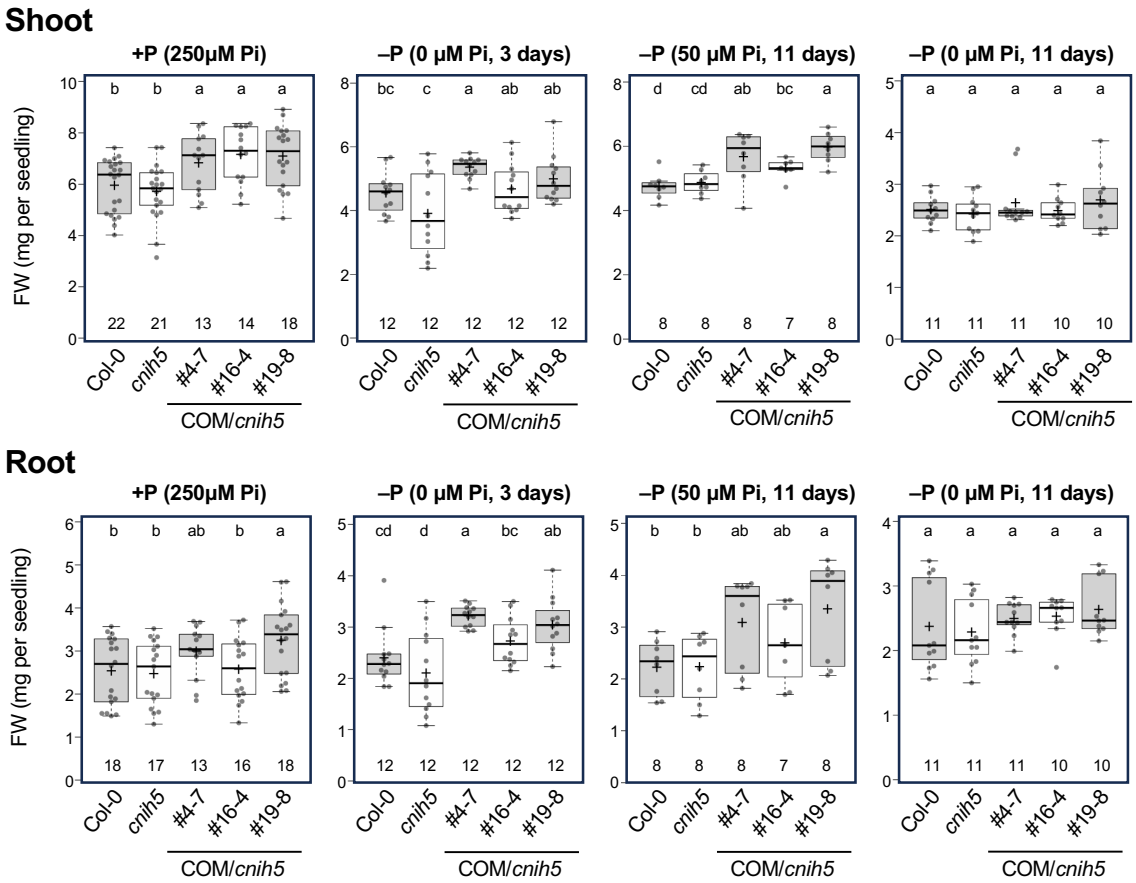

Figure 8. Increasing *in-situ At*CNIH5 expression/activity boosts plant growth.
The shoot and root fresh weight (FW) of *Arabidopsis* 11-day-old WT, *cnih5* and *AtCNIH5pro*: GFP-*AtCNIH5/cnih5* complementation (COM) lines under Pi-sufficient (+P, 250 µM KH_2PO_4), modest Pi-deficient (–P, 0 µM KH_2PO_4, three days of starvation or 50 µM KH_2PO_4, eleven days of starvation), and severe Pi-deficient (–P, 0 µM KH_2PO_4, eleven days of starvation) conditions. Data are visualized using BoxPlotR . Center lines show the medians; the central plus signs (+) show the means; box limits indicate the 25th and 75th percentiles; whiskers extend to the 5th and 95th percentiles, and data points are plotted as dots. Data significantly different from the other groups are indicated by different lowercase letters (n, pools of seedings from independent experiments; One-Way ANOVA, Duncan's test).

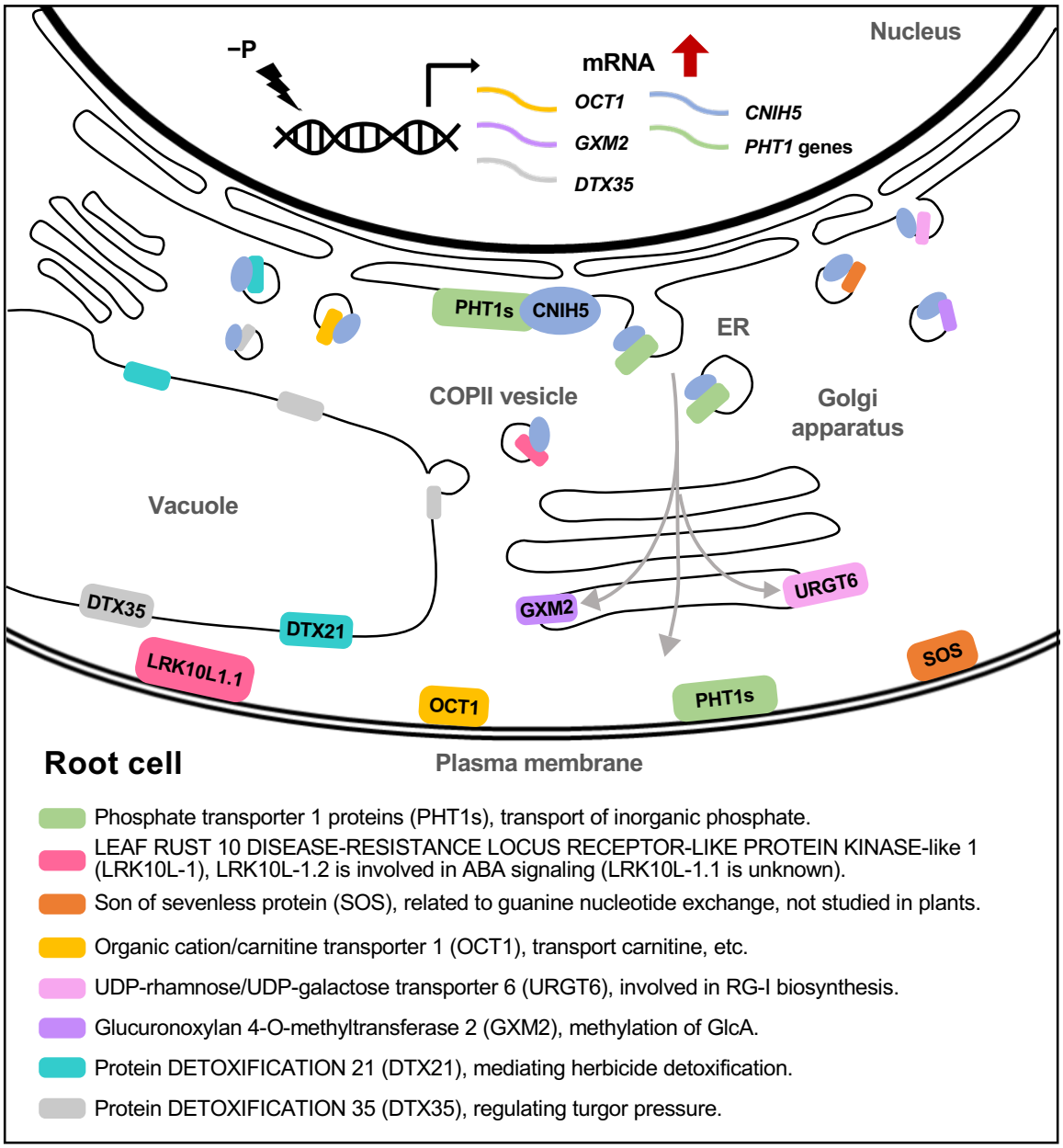

Figure 9. *At*CNIH5-mediated ER-to-Golgi transport of membrane proteins associated with Pi starvation responses in *Arabidopsis* root.

Under Pi starvation (−P), the transcripts of *CNIH5*, *PHT1* genes, *OCT1*, *GXM2*, and *DTX35* increase in *Arabidopsis* root cells . As an ER cargo receptor, CNIH5 assists the ER export of the newly synthesized PHT1s, LRK10L-1.1, SOS, OCT1, URGT6, GXM2, DTX21, and DTX35 and their loading into COPII vesicles, thus their corresponding subcellular destinations.

Table 1. Summary of *At*PHT1s and *At*PHF1 expression in Pi-limited WT and *cnih5* roots.
The normalized ratios compared the protein expression in Col-0_1, Col-0_2, *cnih5*_1 and *cnih5*_2 samples. The FDR adj. *p*-values were in the parentheses.

Accession	Gene name	AGI code	Coverage [%]	Unique peptides	*cnih5*_1 /Col-0_1	*cnih5*_2 /Col-0_1	*cnih5*_1 /Col-0_2	*cnih5*_2 /Col-0_2
Q8VYM2	*AtPHT1;1*	AT5G43350	38	2	0.63 (0.41)	0.54 (0.28)	0.65 (0.31)	0.56 (0.22)
Q96243	*AtPHT1;2*	AT5G43370	30	1	0.61 (0.05)	0.97 (1.00)	0.78 (0.47)	1.24 (0.67)
O48639	*AtPHT1;3*	AT5G43360	10	2	0.58 (0.00)	0.65 (0.24)	0.56 (0.00)	0.74 (0.14)
Q96303	*AtPHT1;4*	AT2G38940	12	6	0.77 (0.40)	0.86 (0.89)	0.79 (0.06)	0.70 (0.00)
Q8GYF4	*AtPHT1;5*	AT2G32830	6	2	0.82 (0.78)	0.73 (0.58)	0.90 (0.87)	0.80 (0.42)
Q9S735	*AtPHT1;9*	AT1G76430	5	2	1.00 (0.99)	1.79 (0.20)	1.27 (0.79)	2.88 (0.00)
Q8GYE0	*AtPHF1*	AT3G52190	40	13	1.45 (0.05)	1.37 (0.36)	1.16 (0.48)	1.14 (0.62)

Coverage [%]: The percentage of the protein sequences covered by identified peptides.

Unique peptides: The total number of distinct peptide sequences unique to the protein group.

Table 2. List of the 31 downregulated microsomal transmembrane proteins in Pi-limited *cnih5* roots.
The normalized ratios compared the protein expression in Col-0_1, Col-0_2, *cnih5*_1 and *cnih5*_2 samples. The FDR adj. *p*-values were in the parentheses. The candidates highlighted in gray were selected for testing protein–protein interaction in this study. Subcellular localization is predicted or annotated by SUBA5, UniprotKB or experimental data.

AGI code	Accession	Gene name	*cnih5*_1/ Col-0_1	*cnih5*_2/ Col-0_1	*cnih5*_1/ Col-0_2	*cnih5*_2/ Col-0_2
		ER				
AT1G04220	Q5XEP9	3-ketoacyl-CoA synthase 2 (*AtKCS2*)	0.73 (0.57)	0.72 (0.66)	0.99 (0.99)	0.98 (1.00)
AT1G34130	Q9FX21	Dolichyl-diphosphooligosaccharide--protein glycosyltransferase subunit STT3B (*AtSTT3B*)	0.75 (0.53)	0.65 (0.30)	0.91 (0.91)	0.77 (0.38)
AT1G51740	P59277	Syntaxin-81 (*AtSYP81*)	1.18 (0.97)	0.73 (0.88)	0.94 (0.98)	0.58 (0.52)
AT3G23175	Q8GYI3	HR-like lesion-inducing protein-like protein	0.68 (0.23)	0.69 (0.46)	0.94 (0.97)	0.96 (0.99)
AT3G23190	Q9LTC9	HR-like lesion-inducing protein-like protein	0.94 (0.99)	0.63 (0.20)	0.92 (0.92)	0.62 (0.00)
AT3G48570	Q9SMP2	Protein transport protein Sec61 subunit gamma-3 (*AtSEC61G3*)	0.72 (0.30)	0.69 (0.42)	0.71 (0.02)	0.72 (0.12)
AT4G14420	O23298	HR-like lesion-inducing protein-like protein	0.76 (0.53)	0.61 (0.07)	0.81 (0.30)	0.64 (0.00)
AT5G43760	Q9FG87	3-ketoacyl-CoA synthase 20 (*AtKCS20*)	1.03 (1.00)	0.60 (0.54)	1.23 (0.93)	0.72 (0.80)
		Golgi				
AT1G34020	Q9FDZ5	UDP-rhamnose/UDP-galactose transporter 6 (*AtURGT6*)	0.60 (0.49)	0.45 (0.18)	0.68 (0.69)	0.50 (0.27)
AT2G03480	Q3EC77	QUASIMODO2 LIKE 2 (*AtQUL2*)	0.78 (0.73)	0.64 (0.35)	0.87 (0.86)	0.68 (0.27)
AT2G40380	Q9SIY7	Prenylated Rab acceptor 1 (PRA1) family protein B2 (*AtPRA1B2*)	0.66 (0.26)	0.74 (0.72)	0.94 (0.97)	1.05 (0.99)
AT4G09990	Q9T0F7	Glucuronoxylan 4-O-methyltransferase 2 (*AtGXM2*)	0.71 (0.76)	0.73 (0.87)	0.58 (0.36)	0.60 (0.54)
AT4G30440	Q9M0B6	UDP-glucuronate 4-epimerase 1 (*AtGAE1*)	0.83 (0.93)	0.64 (0.58)	0.88 (0.93)	0.68 (0.38)
AT4G38270	Q0WQD2	Galacturonosyltransferase 3 (*AtGAUT3*)	0.87 (0.92)	0.62 (0.32)	0.95 (0.98)	0.69 (0.17)
AT5G25100	Q9C5N2	Transmembrane 9 superfamily member 9 (*AtTMN9*)	0.73 (0.69)	0.81 (0.89)	0.70 (0.33)	0.78 (0.62)
		Vacuole				
AT1G33110	Q8W488	Protein DETOXIFICATION 21 (*AtDTX21*)	0.52 (0.00)	0.76 (0.77)	0.48 (0.00)	0.71 (0.40)
AT4G17340	Q41975	Tonoplast intrinsic protein 2;2 (*AtTIP2-2*)	0.88 (0.95)	0.91 (0.97)	0.65 (0.34)	0.64 (0.40)
AT4G25640	F4JTB3	Protein DETOXIFICATION 35 (*AtDTX35*)	0.86 (0.89)	0.66 (0.31)	0.89 (0.83)	0.68 (0.02)
AT5G46090	Q9FNL3	DUF679 domain membrane protein 6 (*AtDMP6*)	0.74 (0.39)	0.64 (0.22)	0.86 (0.65)	0.74 (0.17)
		PM				
AT1G05570	Q9AUE0	Callose synthase 1 (*AtCALS1*)	0.74 (0.60)	0.73 (0.66)	0.82 (0.72)	0.80 (0.75)
AT1G17620	Q9LNP3	Late embryogenesis abundant (LEA) hydroxyproline-rich glycoprotein family	0.73 (0.54)	0.61 (0.23)	0.93 (0.96)	0.78 (0.68)
AT1G18390	P0C5E2	LEAF RUST 10 DISEASE-RESISTANCE LOCUS RECEPTOR-LIKE PROTEIN KINASE-like 1.2 (*AtLRK10L-1.2*)	0.74 (0.35)	0.72 (0.53)	0.75 (0.09)	0.73 (0.15)
AT1G26650	Q9LQY7	Son of sevenless protein (*AtSOS*)	0.61 (0.22)	0.70 (0.70)	0.61 (0.09)	0.70 (0.27)
AT1G73220	Q9CAT6	Organic cation/carnitine transporter 1 (*AtOCT1*)	0.89 (0.93)	0.86 (0.93)	0.73 (0.04)	0.69 (0.05)
AT2G27140	Q9ZVC6	HSP20-like chaperones superfamily protein	1.00 (0.99)	0.61 (0.13)	1.11 (0.87)	0.65 (0.01)
AT3G02600	Q8LFD1	Lipid phosphate phosphatase 3 (*AtLPP3*)	0.89 (0.92)	0.62 (0.16)	0.97 (0.98)	0.68 (0.02)
AT3G61270	Q9M2D7	Glycosyltransferase (*AtT20K12.170*)	0.84 (0.89)	0.67 (0.46)	0.80 (0.58)	0.64 (0.13)
AT4G01830	Q9SYI3	ATP binding cassette (ABC) transporter B family member 5 (*AtABCB5*)	0.75 (0.79)	0.68 (0.71)	0.99 (1.00)	1.03 (1.00)
AT5G20970	F4K6X6	HSP20-like chaperones superfamily protein	0.85 (0.86)	0.51 (0.00)	1.10 (0.89)	0.66 (0.01)
AT5G43350	Q8VYM2	Inorganic phosphate transporter 1;1 (*AtPHT1;1*)	0.63 (0.41)	0.54 (0.28)	0.65 (0.31)	0.56 (0.22)
AT5G43360	O48639	Inorganic phosphate transporter 1;3 (*AtPHT1;3*)	0.58 (0.00)	0.65 (0.24)	0.56 (0.00)	0.74 (0.14)